Rapid changes of dust geochemistry in the Saharan Air Layer linked to sources and meteorology

Sergio Rodríguez[1,2,3,*], Giulia Calzolai[4], Massimo Chiari[4], Silvia Nava[4], M. Isabel García[1,5], Javier López-Solano[1], Carlos Marrero[1], Jessica López-Darias[3,5], Emilio Cuevas[1], Silvia Alonso-Pérez[6], Natalia Prats[1], Fulvio Amato[7], Franco Lucarelli[4,8], Xavier Querol[7]

1. Izaña Atmospheric Research Centre, AEMET, Tenerife, Spain
2. Estación Experimental de Zonas Aridas EEZA CSIC, Almería, Spain
3. Instituto de Productos Naturales, IPNA CSIC, Tenerife, Spain
4. Istituto Nazionale di Fisica Nucleare, Firenze, Italy
5. Department of Chemistry, University of La Laguna, Spain
6. Universidad Europea de Canarias, Tenerife, Spain
7. Institute of Environmental Assessment and Water Research, IDAEA-CSIC, Barcelona, Spain
8. Physics Department, University of Florence, Italy

*email: <sergio.rodriguez@csic.es>

Abstract

Based at Izaña Observatory (~2400 m a.s.l. in Tenerife), we performed 1-hour resolution measurements of elemental composition of dust in the Saharan Air Layer (SAL) and studied the variability of the ratios of these elements to aluminium (elemental ratios). In a period (~1 week) of continuous dust presence (50-200 μg/m^3), we observed rapid variations of dust composition; some elemental ratios changed by a factor 2 in a few (5 to 8) hours. The lowest variability (Normalized Variability Range, %) was found for Si/Al (9%) and Fe/Al (9%), followed by the ratios of K, Ti, Mg, Mn, Ca and Sr to Al (20 to 80 %), and the highest for S/Al, Na/Al and Cl/Al (110 to 160 %) and a number of trace metals (Cr, Cu, Ni, Zn, Zr) and Br (>200%). This variability was induced by the alternating impacts of three of the large North African dust sources: NE Algeria (rich in evaporite minerals bearing Ca, S, Sr, K and Mg and in illite mineral), Western Sahara to Bechar region (containing Na, S and Cl rich Yermosol soils) and SW Sahara – Western Sahel (rich in illite and hematite). We traced the variability in large-scale meteorology using the so-called North African Dipole Intensity (NAFDI: strength of the subtropical Saharan high -Morocco- to the monsoon tropical low -Nigeria-). The mobilization of dust from the different sources was associated with westward propagating Harmattan pulses linked to the change of phase of NAFDI (- to +), the associated westward shifts of the Saharan Heat Low and convective monsoon inflow. We found a correlation between dust composition in the SAL and NAFDI: moderate NAFDI values (0 to +2.5) were associated with Ca, K, Na, Mg and S

rich dust linked to dust sources in NE Algeria, whereas higher NAFDI values (+2.5 to +4) were linked to Fe rich dust (Ca, Na and S depleted) linked to dust sources in SW Sahara – Western Sahel. The results of this study also show that some trace elements (Br, Cr, Ni, Zn and Zr) are influenced by industrial emissions into North Africa.

Keywords: *Saharan Air Layer, Saharan dust sources, dust geochemistry, North Africa, Harmattan, NAFDI*.

1. Introduction

Desert dust emitted from soil by the action of wind is the second most abundant atmospheric aerosol after sea salt (Andreae and Rosenfeld, 2008). Dense dust plumes occur over thousands of kilometres beyond their desert source regions (Prospero et al., 2002). This has implications on radiative fluxes (Miller et al., 2014), cloud formation and properties (Boose et al., 2016), nutrients deposition on ecosystems (Ravelo-Pérez et al., 2016) and human health (Zhang et al., 2016). Dust is a mixing of tens of minerals (Kandler et al., 2009; Reid et al., 2003), each presenting physical and chemical properties which modulate dust impacts, e.g. feldspars are active ice nuclei (Atkinson et al., 2013), hematite absorb UV radiation (Alfaro et al., 2004), carbonates neutralize acid pollutants (Ito and Feng, 2010), whereas iron bearing clays and oxides provide iron to ecosystems (Rizzolo et al., 2017). Some models are already including such mineral diversity (e.g. Nickovic et al., 2012; Perlwitz et al., 2015). Experimental methods still have limitations for quantifying the long-term variability of dust mineralogy, thus complementary elemental composition data is being used (Rodríguez et al., 2012), even for model validation (Pérez García-Pando et al., 2016).

North Africa is the largest and most active dust source region, accounting for 50 to 70 % of global emissions (Huneeus et al., 2011). In summertime, dust is uplifted to high altitude (Cuesta et al., 2009). Then exported in the Saharan Air Layer (SAL; Prospero and Carlson, 1972), i.e. the dusty airstream that flows over the North Atlantic at altitudes 1 - 5 km a.s.l. off North Africa and at < 2 km.a.s.l. over the Caribbean (Tsamalis et al., 2013). Dust sources are mostly located in topographic lows, associated with drainage of ancient watercourses and endorheic basins (Prospero et al., 2002) where fluvial sediments accumulated during the so-called African Humid Periods (De Menocal and Tierney, 2012; Middleton et al., 2018; Skonieczny et al., 2015). The variability of soil dust composition across the North African sources is a topic of major interest; however in-situ aerosol measurements are scarce (Scheuvens et al., 2013) and proxies based on dust mineralogy in specific site extrapolated using the FAO Soil Map of the World are being used (Claquin

et al., 1999; Nickovic et al., 2012; Journet et al., 2014; Pérez García-Pando et al., 2016). The variety of dust sources impacting in distant regions has also been identified with isotopic characterization (Bozlaker et al., 2018).

The variability of dust composition in the SAL (Kandler et al., 2007; Rodríguez et al., 2011) may also depend on meteorology, more specifically (i) on the occurrence of the specific meteorological scenarios activating dust emissions (Fiedler et al., 2013; Flamant et al., 2007), prompting regional dust mobilization (Schepanski et al., 2017) and dust export to the Atlantic (Jones et al., 2003; Tsamalis et al., 2013), and (ii) on wind speed, which influences the deposition rates of the minerals linked to the coarser dust fractions. Meteorology linked to dust export in summertime, and its connection to climate related processes (monsoon, Saharan Heat Low, etc...), is a topic of major interest (Engelstaedter and Washington, 2007; Evan et al., 2016; Cuevas et al., 2017; Schepanski et al., 2017).

This study addresses three questions: how quick does dust composition change in the SAL?, what is the connection to dust sources?, and what is the role of meteorology?. We address these questions by performing temporal high resolved measurements of elemental composition of dust in the high altitude Saharan Air Layer.

2. Methods

2.1 Aerosol samples

In this study we analysed a data set of 1-hour time resolution measurements of elemental composition of aerosol samples collected at Izaña Observatory in Tenerife, located at 2400 m.a.s.l. The samples were collected from 23-Aug 19h to 30-Aug 17h 2010. The hourly resolution sampling was performed with two streakers (D'Alessandro et al., 2003): one to collect samples of total particulate matter (PM_T) and another one to collect samples of coarse (2.5-10 μm) and fine (< 2.5 μm) aerosol fractions, i.e. $PM_{2.5-10}$ and $PM_{2.5}$, respectively. A total of 166 hourly samples were collected with each streaker. PM_T and $PM_{2.5}$ are collected on polycarbonate membranes while $PM_{2.5-10}$ is collected by impaction on thin Kapton® foils. Here in after we will refer to PM_T, $PM_{2.5-10}$ or $PM_{2.5}$ as PM_x. We used this dataset to study the variability of dust composition, the potential dust sources in North Africa and the relationship between variability of dust composition and meteorology.

A second dataset, based on sampling from 1-Aug to 31-Aug 2013 (sampling from 22h to 08h), was used to assess if the relationship between variability of dust composition and meteorology observed in 2010 was also observed in other summers. This additional data set includes the elemental composition of PM_{10} aerosols collected on Teflon 47 mm filters at an airflow of 2.3 m^3/h. Bulk PM_{10} concentrations were determined by gravimetry,

by conditioning the filters at 20 °C following the EN-14907 procedure (except that RH was kept to 30% instead of 50%).

The data set used in this study is available at Rodríguez et al. (2019).

2.2 PIXE analysis

PM_x samples collected at Izaña have been analysed by Particle Induced X-ray Emission (PIXE) and Particle Induced Gamma-ray Emission (PIGE) at the Tandetron accelerator of the LABEC-INFN laboratory (Florence, Italy), where a specific, high efficiency PIXE-PIGE set-up has been developed for the analysis of aerosol samples (Lucarelli et al., 2014, 2018, Calzolai et al., 2015).

Each sample was irradiated with a 3.0 MeV proton beam (10-150 nA intensity) for 60-90 s. For Teflon samples, a filter scanning was carried out to analyse most of the deposit area, while hourly samples were analysed by a properly collimated beam, which scanned the deposit in steps corresponding to 1 h of aerosol sampling, thus providing the elemental concentrations with hourly time resolution (Calzolai et al., 2015).

PIXE spectra were fitted using the GUPIX code (Maxwell et al., 1995) and elemental concentrations (Na, Mg, Al, Si, P, S, Cl, K, Ca, Ti, V, Cr, Mn, Fe, Ni, Cu, Zn, As, Se, Br, Rb, Sr, Zr, Mo, Ba, Pb) were obtained by a calibration curve from a set of thin standards (Micromatter Inc.). The lighter elements (Na, Mg, Al and Si) concentrations were corrected for self-absorption effects using experimental corrective factors obtained by PIGE measurements of Na and Al (Calzolai et al., 2010; Formenti et al., 2010). Detection limits are within 1-10 ng/m^3 for elements from Na to V and 1 ng/m^3 for elements from Cr to Pb. A verification of the overall accuracy was made by analysing the NIST SRM 2783 standard (Air Particulate on Filter Media).

It is worth noting that PIXE is an appropriate technique for the study of particulate matter, as it is multielemental, rapid, very sensitive, not destructive, and it does not require any sample pre-treatment. In particular it is very effective for the study of mineral dust as it is particularly sensitive for the detection of medium Z elements, including important soil related elements, such as Al, Si, K, Ca, Ti, Sr, Mn and Fe.

Bulk dust concentration was determined by considering that Al accounts for 8% of dust in the Earth Crust (Mason, 1966). This is consistent with our observations: see the slope of Al versus bulk dust in PM_{10} determined by gravimetry (Fig. 1A). These PM_{10} samples are basically constituted by dust, as their ochre colour indicates (Fig. 1B).

147 2.3 Potential Source Areas of dust

148 The Potential Source Areas of dust were identified by analysing the "Median Ratios
149 At Receptor" plots, determined for the ratio of each element (X) to Al (X/Al), based on the
150 elemental composition of dust at Izaña receptor site and backtrajectories. These plots
151 represent the median ratio of each X/Al measured at the receptor site (Izaña in this study)
152 when the air mass has previously passed above each 1◦ × 1◦ degree pixel over North Africa
153 (e.g. Fig. 4, discussed below). Back-trajectories were calculated with HYSPLIT software
154 (Stein et al., 2015) using GDAS data. A total of 166 back-trajectories were calculated, one
155 for each hour observation of aerosol composition based on the streaker sampling: 23-Aug
156 19h to 30-Aug 17h 2010 (Fig. 1C). The identification of the Potential Source Areas (based
157 on Median Ratios At Receptor plots analysis; Fig.4) was performed only during the period
158 when Izaña was within the dusty SAL (dust > 40 μg/m^3; 24-Aug 11h to 30-Aug 17h 2010);
159 the back-trajectories density map (number of back-trajectory points that passed by each
160 1◦ × 1◦ degree pixel of the study domain) of this period is shown in Fig. 1D. In this group
161 (Fig 1D), the median value of the X/Al ratios was calculated for each 1◦ × 1◦ degree pixel
162 (Fig.4), only if at least 5 back-trajectories pass by that pixel. This calculation method of the
163 Median Ratios At Receptor is similar to that used by Rodríguez et al. (2011) for studying
164 the potential source areas of the pollutants observed in the dusty SAL and by García et al.
165 (2017) for studying the transatlantic transport of dust and aerosol pollution from North
166 America in the westerlies. This method does not use the vertical wind component. We
167 performed several tests, and calculated the MRAR plots considering only the back-
168 trajectories points located at low altitude (below certain threshold altitudes). Results did
169 not differ significantly from those obtained without limiting the altitude of the back-
170 trajectories (not shown for the sake of brevity).
171
172 2.4 Meteorology and satellite dust observations

173 Meteorology was studied using the NCEP/NCAR re-analysis data (Kalnay et al.,
174 1996), whereas satellite Dust Optical Depth observations (dark target + deep blue MODIS
175 combination) were provided by the Giovanni system of NASA (Levy et al., 2010; Hsu et al.,
176 2013). For studying some events, the hourly images and Dust Optical Depth (Brindley and
177 Russell, 2009; Legrand et al., 2001) measured by the Spinning Enhanced Visible and Infra-
178 Red Imager (SEVIRI) radiometer boarded on Meteosat Second Generation and compiled
179 by the WMO-SDSWAS portal (https://sds-was.aemet.es/forecast-products/dust-
180 observations/) were also used.
181
182

3. Results and discussion

Figure 2A illustrates how the dusty SAL impacted over the North Atlantic in the study period. Figure 2C shows the so-called Potential Source Areas of North African dust that may influence dust composition, according to Scheuvens et al. (2013), whereas Figure 2D-2I shows the meteorological fields (described below) that illustrate the complex summer meteorological scenario in North Africa. The positive correlation observed between dust at Izaña and Harmattan wind speed (central Algeria), during 30 years (Fig. 2B), illustrates the key role of meteorology in the processes involved in dust export. We studied the links between the variability of dust composition in the SAL (Fig.2A), dust sources (Fig. 2C) and meteorology (Fig. 2D-2I).

3.1 Temporal variability of dust composition

Fig. 3A shows 1-hour resolution measurements of dust concentration at Izaña Observatory (Tenerife), from 23-Aug 19h to 30-Aug 17h 2010. Izaña is located above the marine boundary layer, and directly exposed to the dusty SAL (see details in Rodríguez et al., 2015). Although three size fractions were independently measured (PM_T, $PM_{2.5-10}$ and $PM_{2.5}$) for simplicity, we perform our descriptions just in terms of total dust ($dust_T$). Initially (23-Aug 19h to 24-Aug 02h) $dust_T$ concentrations were low (~15 μg/m^3), but increased from 18 to ~70 μg/m^3 on 24-Aug (02h to 22h; Fig.2A). During most of the sampling period (~6 days: 24-Aug 11h to 30-Aug 17h) Izaña Observatory was permanently impacted by the dusty SAL (Fig. 2A), with $dust_T$ concentrations ranging from 40 to 200 μg/m^3 (Fig. 3A). Fig. 3B-3I shows the ratios of Ca, S, Mg, Cl, Na, K, Si and Fe to Al when Izaña was impacted by the SAL.

In order to compare the mean aerosol composition with the mean composition of soil dust, we determined the Enrichment Factor (EF), using Al as tracer and the average upper continental crust composition of Mason (1966). Results support the idea that the analysed elements of the aerosol population in the SAL were dominated by soil desert dust. On average we found low EFs (0.5 to 2) for most of the study elements (Ni, Na, Si, Cu, K, Mn, Zr, Fe, Mg, Sr, Ca, Ti, P, Zn and Cr). As average, dust was slightly depleted in Na, Si, K and Mn, and slightly enriched in Sr, Ca, Ti and P. The highest EFs were found for Br (30 to 60 in the different size ranges), S (~ 20 to 65) and Cl (40-45). Trace metals (Ni, Cr, Zn and Zr) showed higher EF in the fine (2 to 4) than in the coarse and total (< 2) fractions. These results of the EF are consistent with the ochre colour of the samples (Fig.1B) and the slope of Al versus PM_{10} (8%, Fig. 1A; similar to the mean content of Al in the Earth Crust).

Dust composition in the SAL experienced a significant variability, traced by the ratios of some elements to Al, e.g. those of Ca, S, Mg, Cl, Na, K and Fe (Fig. 3B-3I). The ratio

Ca/Al changed by a factor ~2 in a few (5 to 8) hours. Top of Fig.3B highlights some events (E1 to E6) discussed below, e.g. pulses of Ca rich dust occurred around 25-Aug ~00h (event E1), the 27-Aug around 07h (E4) and the 29-Aug at 23h (E6; Fig. 3B). Pulses of dust rich in other elements were also recorded (Fig. 3C-3I).

We quantified the variability of dust composition by determining the NOrmalized VAriability Range (NOVAR) of each ratio to aluminium, defined as:

$$NOVAR = 100 \cdot (P98^{th} - P2^{nd}) / average \qquad Eq\text{-}1$$

where the average (arithmetic mean), the percentile 98th (P98th) and the percentile 2nd (P2nd) refer to the ratio X/Al in the dust samples collected in the SAL. The values of X/Al (Table 1) are within the range of those observed in other studies (Rodríguez et al., 2011 and references within). The lowest variability was found for Si/Al (NOVAR: 9%) and Fe/Al (9%), followed by X/Al of key dust components, such as Ti, K, Mg, Mn, Ca and Sr (20 to 80 %) and S, Na and Cl (111 to 156 %). Trace elements, as Cr, Ni, Cu, Zn, Br and Zr, showed high X/Al NOVAR values (107 to 277%).

3.2 Dust source regions

We assessed how dust composition in the SAL (Fig. 3) (i.e. the X/Al) changes depending on the source region of dust. We determined the Median Ratios At Receptor (MRAR) plots, which represents the typical (median) X/Al of a given element measured at Izaña receptor site when the air mass has passed (according to back-trajectories; Fig. 1C) by each 1°x1° pixel of the study domain (Fig.4). The MRAR (Fig.4) allows identifying (i) source areas of aerosols and (ii) transport pathways from the source to the receptor site, especially when there are very few and small sources. The airstream that may influence the transport pathways in North Africa are illustrated with the arrows shown in Fig 1C. The potential influence of the industrial emission on trace elements was also assessed (location of industrial sources shown in Fig. 1D, according to Rodríguez et al., 2011). We determined the MRAR only using the data collected when Izaña was impacted by the dusty SAL (dust > 40 μg/m^3; 24-Aug 11h to 30-Aug 17h 2010). The plots show that the X/Al of:

- Si, Fe and Mn are high when dusty air arrives from southern Sahara (Fig.4A, 4C and 4E),
- Ca, Sr, S, K and Mg are high when dust arrives from northeast Algeria (Fig.4B, 4D, 4F, 4K and 4H),
- Na are Cl are high when dust airflow arrives from northwest Algeria (Fig.4G and 4I),

- trace elements (Br, Cr, Ni, Zn and Zr) shows transport pathways from regions affected by industrial emissions in Tunisia, Algeria and Morocco (Fig. 4M-4Q),

Our results were compared with the location of the so-called Potential Source Areas (PSAs) proposed by Scheuvens et al. (2013) as results of a literature review. These PSAs are plotted in Fig. 2C1 and 2C2 to highlight their location in topographic lows, some of them associated with the watersheds (Skonieczny et al., 2015). Briefly: (1) PSA1 expands over Northeast Algeria and Tunisia; (2) PSA2 is placed south of Atlas mount, along the northern side of the Tamanrasset paleo-river (ending in Arguin bay, Mauritania); (3) PSA3 is located east of Hoggar massif, throughout the southern part of the Tamanrasset paleo-river and the northern part of the Niger river basin; (4) PSA4 is the northern slope of Tibesti massif, and (5) PSA5 is the Bodele depression.

Fig. 5 shows the scatter plot of some elements (Ca, Sr, S, Na, Cl, Si and Fe) to Al, indicating the slope of the different trending groups. In order to put our results in the context of the considered key large-scale dust sources (Scheuvens et al., 2013), the median X/Al value measured at Izaña when the air masses have passed by the PSAs 1 to 3 is shown in Table 2, even if the spatial variability of dust composition is most probably not limited to these PSAs (Nickovic et al., 2012; Journet et al., 2014). The X/Al ratios in some key Si-Al bearing minerals (Table 3) will be used to discuss the regional variability we observe in dust composition (Fig.4). The location of the industrial areas in North Africa (with potential emissions of trace elements) is shown in Fig. 1D.

3.2.1. Group -1: Ca, Sr, S, K, Mg

These elements show a high X/Al in PSA1. Main features:

- Ca/Al has a high variability (NOVAR = 78%; Table 1). The scatter plot of Ca vs Al shows two main groups of dust particles: Ca depleted (ratio, slope - S1 = 0.39; Fig. 5A1) and Ca rich (S2 = 0.68; Fig. 5A1). Ca rich dust is observed in PSA1 (ratio to Al ~ 0.62; Fig.4B), whereas PSA3 (~0.40) is Ca depleted. This variability also occurs in the coarse and fine fractions (Fig. 5A). The rather high ratio of Ca/Al (~ 0.5) observed in northern PSA2 is probably influenced by a transport pathway from PSA1 (Fig. 4B). A hot spot rich in Ca is also observed in inner Morocco (in-Mo, a Potential Source Area to which we will refer as PSA-in-Mo-), where Ginoux et al. (2012) attributed dust emissions to anthropogenic use of soil (probably the agriculture fields western of Marrakesh, which match with the location of PSA-in-Mo pointed in Fig.4B. Ca mostly occurs in calcite ($CaCO_3$) and gypsum/anhydrite ($CaSO_4 \cdot 2H_2O$ / $CaSO_4$), and secondarily as dolomite ($(CaMg)_2CO_3$) and anorthite ($CaAl_2Si_2O_8$). The first two evaporite minerals are abundant in PSA1 and 2, and

scarce in PSA3 (according to the soil mineralogical maps of Nickovic et al., 2012 and Journet et al., 2014), a distribution consistent with our observations (Fig. 4B) and with those of Kandler et al. (2007).

- Sr/Al has a NOVAR=87% (Table 1). Roughly two types of dust particles are observed: Sr depleted (S1 = 4.0 $\cdot 10^{-3}$; Fig. 5B1) in PSA3 (Fig.4D) and Sr rich (S2 = 6.2 $\cdot 10^{-3}$; Fig. 5B1) near PSA1 (Fig. 4D). The spatial distribution resembles that of Ca, with high levels in PSA1, northern PSA2 and In-Mo. This Sr-Ca co-variability is probably due to the fact that Sr has a high geochemical affinity with Ca and uses to substitutes it in calcite and gypsum ($CaSO_4 \cdot 2H_2O$). A similar Sr-Ca co-variability was found by Moreno et al. (2006).
- S/Al shows a very high variability (NOVAR = 111%; Table 1). Two trends are observed: S poor (slope = 0.06; Fig.5C1) dust in PSA3 (Fig.4D) and S rich (slope = 0.15; Fig.5C1) dust in PSA1, northern PSA2 and In-Mo (Fig.4D). The aerosol samples collected (under dust free conditions) from 23-Aug 19h to 24-Aug 10h were not included in this analysis (i.e. neither Fig. 4 and Table 1); they showed a much higher S/Al ratio (S3 = 0.44; Fig 5C1) attributed to the transport of fine sulphate pollution (Fig. 5C3) from the Mediterranean (back trajectories not shown for the sake of brevity). Sulphur is usually present as gypsum/anhydrite in soil dust, with higher amounts in PSA1 and 2, and lower in PSA3 (Claquin et al., 1999).
- Mg/Al showed a smoother variability (NOVAR=25%), with typical ratios between 0.23 and 0.29 (Table 1), slightly higher than that characteristic of the illite (Table 3), a dominant clay in North African dust (Reid et al., 2003). Mg also occurs in dolomite ($CaMg)_2CO_3$), and other clays (e.g. chlorite, vermiculite) and feldspars (Table 3). The presence of Ca-Mg carbonate (dolomite) in northern Algeria (Fig. 4B), accounts for the observed Mg rich dust in PSA1 (0.28) compared to PSA2 and PSA3 (0.24; Fig. 4H).
- K/Al also has a smooth variability (NOVAR=25%; Table 1). A northward gradient is observed, with values < 0.20 south of 25°N, and the highest ratios (0.22) in PSA1 (Fig. 4K). The high K/Al ratio in PSA1 (Fig.4K) is consistent with the atlases that report the presence of soils rich in illite in this specific area (Nickovic et al., 2012), a clay mineral characterised by a high K/Al ratio (=0.67; Table 3), that contributes to increase the K/Al ratio.

The dust rich in Ca, S, Sr, K and Mg in PSA1 are associated with a Cretaceous limestone-rich basement, also rich in illite (Nickovic et al., 2012), and with the occurrence of dusty dry lakebeds, so-called chotts, where evaporite minerals (rich in Ca, Na, Sr, K

carbonates and sulphates) occur (Hamdi-Aissa et al., 2004 and references within Rodríguez et al., 2011). Dust emission in this region, where the chotts Felrhir and Melghir (eastern Algeria) and the chotts el-Djerid and el-Gharsa (Tunisia) are located, is detected by satellite (Prospero et al., 2002). Its impact in the SAL was described by Rodríguez et al.(2011).

3.2.2. Group -2: Na and Cl

Na/Al and Cl/Al exhibit a high NOVAR (116% and 156%, respectively; Table 1) and a northward gradient, with the highest values along the northern PSA2 (ratio ~ 0.3 for Na and ~ 0.14 for Cl; Table 2), compared to PSA3 (ratio ~ 0.15 for Na and ~ 0.05 for Cl; Fig. 4G and 4I). There are some hot spots rich in these elements in PSA1 (ratio ~ 0.27 for Na and ~ 0.10 for Cl; Fig. 4G and 4I). The slope of Na vs Cl (~2.2, $r^2 = 0.92$) is much higher than that in sea salt (which typically ranges from 0.5 to 0.6) and this discards marine emissions as the main source of Na. This is consistent with the observations of Prospero and Carlson (1972), who showed that sea salt is not present in the SAL because the airstream lies above the marine boundary layer. The scatter plots give evidence for the occurrence of two types of dust particles: depleted (S1 = 0.17 for Na and S1 = 0.05 for Cl) and enriched (S2 = 0.31 for Na and S2 = 0.11 for Cl) in these elements (Fig.5D and Fig.5E). Northern PSA2 is characterised by Halip Yermosol soil (Nickovic et al., 2012), a FAO category for Na-rich saline lands, which in this region occurs around the abundant sebkhas (Rodríguez et al., 2011), where precipitated Na-sulphate, Na–carbonate and NaCl evaporites are dust components (Fehlberg and Stahr, 1985; Hamdi-Aissa et al., 2004). This is probably the origin of the high Na/Al and Cl/Al ratios in this region (Fig. 4G and 4I). High ratios of none-ammonium sulfate / Al ratios have been observed in the SAL when dust originates in northern PSA2 (Rodríguez et al., 2011).

Dust emission in northern PSA2, Bechar basin, was also identified by Fiedler et al.(2013) and Knippertz et al.(2007). The Na and Cl rich dust in PSA2 is linked to the presence of Yermosol soils, a feature consistent with the hot spots of Ca, S and Sr observed in this region (Fig. 4B, 4D, 4F).

3.2.3. Group -3: Si, Fe and Mn

This group exhibits high X/Al in PSA3 (Fig. 4A, 4C and 4E and Table 2). A hot spot is also observed in PSA1. The ratio of:

- Si/Al varied in a narrow interval (NOVAR = 9%), with values of ~ 2.04, 1.98 and 2.10 in PSAs 1, 2 and 3 respectively (Fig. 4A and Table 2). This narrow variability (Fig. 5F1 and 5F2) is consistent with the results of Reid et al. (2003) and Kandler

et al., (2007), who found that silicon in the SAL was mainly bounded to aluminosilicate. The higher Si/Al in PSA1 and northern-PSA3 is consistent with the mineralogical map that report on soils rich in illite clays in these regions (Nickovic et al., 2012; Journet et al., 2014), a mineral with a high Si/Al ratio (=2.8; Table 3) that contribute to increase the Si/Al ratio in the mineralogical cocktail constituting the bulk dust mass. A similar Si/Al variability, linked to the content of illite, was observed in Cape Verde (Caquineau et al., 1998). Some feldspar, as orthoclase, exhibits high Si/Al ratios (3.12, Table 3), but the soils of northern PSA3 are depleted in these minerals, according to Nickovic et al. (2012). The Si/Al ratios observed in the SAL over the North Atlantic (1.9 to 2.2, according to this study and to Kaldler et al., 2007 in Tenerife; Reid et al., 2003, in Puerto Rico and Caquineau et al., 1998, in Cape Verde) are lower than those observed near the dust sources in North Africa (3 to 6) according to Scheuvens et al. (2013). The quartz in the North African soils mostly occurs in the coarse - silt fraction (Journet et al. 2014), so deposition during long-range transport in the SAL accounts for the observed decreased in the Si/Al ratio. Nonetheless, northern PSA3 soils are rich in quartz (Nickovic et al., 2012), so even if this mineral is present in low amounts in small size fractions (Kandler et al., 2007) it may also contribute to the high Si/Al ratio observed in the dust arriving from this region (Fig. 4A).

- Fe/Al also had a narrow variability (Fig. 5G1-5G3) and a low NOVAR (= 9%), with values ~ 0.48, 0.46 and 0.49 in PSA 1, 2 and 3, respectively (Fig. 4C and Table 2). This variability range is similar to that observed in previous studies (Moreno et al., 2006; Formenti et al., 2008; Scheuvens et al., 2013). Fe is regularly included in (i) Si-Al-bearing minerals (Reid et al., 2003) and (ii) nanoparticles of iron oxides/hydroxides (hematite: Fe_2O_3 and goethite: α-FeO(OH))) attached to the surface of other dust particles (Reynolds et al., 2014; Moskowitz et al., 2016) that contributes to increase the observed Fe/Al in comparison with the Fe/Al ratios in the Si-Al-bearing minerals (0.16 for illite and 0.43 for vermiculite; Table 3). The high Fe/Al ratio we observe in PSA3 (Fig. 4C) is consistent with the mineralogical maps that report on hematite rich soils in western-PSA3 (Journet et al., 2014). The higher Fe vs Al slope in the fine than in coarse fraction (Fig. 5G1-5G3) is consistent with the study of Kander et al. (2007), who found a decrease in the amount of hematite with increasing particle size.
- Mn/Al exhibited a wider variability (NOVAR = 46%), with values ~ 7.9, 7.3 and $8.3 \cdot 10^{-3}$ in PSA 1, 2 and 3 (Fig. 4E and Table 2). Because of its geochemical affinity, Mn may partially replace to Fe in Fe-oxides.

PSA3 is among the most active dust sources in summer (Engelstaedter and Washington, 2007; Flamant et al., 2007; Knippertz, 2008). The high Si/Al and Fe/Al we observe in this dust from this area is consistent with the soils rich in illite and hematite reported for this region (Nickovic et al., 2012; Journet et al., 2014).

3.2.4. Group -4: trace elements

The MRAR plots of Ti, Cu, Br, Cr, Ni, Zn and Zr are shown in Fig. 4J-4P. A detailed analysis is out of the scope of this study, so we did just a brief exploration.

- The ratios of Br, Cr, Ni, Zn and Zr to Al exhibit high values downwind of the main industrial areas of Tunisia, Algeria and Morocco (shown in Fig.1D and Fig.4M), where oil refineries, fertilizing industry, coal power plants and urban areas occur (see details in Rodríguez et al. 2011). The Atlantic coast of Morocco shows high ratios of Br, Cr, Ni, Zn, Ti and Zr to Al (Fig. 4M-4Q). A clear transport pathway of Br, Cr, Ni, Zn and Zr from Hassi Messaoud industrial area, in Eastern Algeria, is observed (Fig. 4M-4Q). Although marine emissions may contribute to Br, anthropogenic emissions (e.g. pesticide application, chemical manufacturing, coal burning, and PVC usage and disposal; Lammel et al., 2002) play a role. A fact that is consistent with the absence of Na-Cl marine sea salt described above.
- Soil emissions may accounts for the high ratios of Ti and Cu to Al in PSA2 (Fig. 4J and 4L).

3.3 Large scale meteorology

In this final section we assess if the day-to-day variability in meteorology in North Africa accounts for the observed temporal variability of dust composition in the SAL (Fig.3) in relation to the location of the dust sources (Fig. 2C and 4).

The summer meteorological scenario in North Africa (Fig. 2D-2I) is characterised by (i) the so-called North African High (NAFH, centred over Northern Algeria at standard levels above 850Pha; Fig. 2G; Font-Tullot, 1950, UK Meteorological Office, 1962), (ii) the InterTropical Convergence Zone (ITCZ) - also so-called Intertropical Discontinuity (ITD, Scott, 1952) – located between 16 and 23 °N (Fig.2A), (iii) the monsoon inflow south of the ITCZ, and (iv) the Saharan Heat Low (SHL; Lavaysse et al., 2009), which results in high temperatures and high thickness of the 1000 – 500 hPa layer (Fig.2H-2I). North (dry side) of the ITCZ, Harmattan (subsiding) wind prevails (Fig.1D-1E), whereas South (wet side) of the ITCZ the (uplifting) monsoon inflow occurs (Fig.1F). Dust emission is associated with the vertical transfer of moment linked to the morning breakdown of low level jets (Fiedler

et al., 2013; Schepanski et al., 2017) and the occurrence of afternoon deep convection cells (Knippertz et al., 2007; Marshman et al., 2008; Schepanski et al., 2017). These emission mechanisms tend to have a meso (and even smaller) scale (Fiedler et al., 2013; Flamant et al., 2007), and they occur embedded in the larger scale patterns involved in the regional dust mobilization (e.g. SHL, Harmattan, monsoon inflow, etc., Allen and Washington, 2013; Engelstaedter et al., 2015) and dust export in the SAL (Jones et al., 2003; Tsamalis et al., 2013).

For studying the variability of dust composition, we traced the variability of the meteorology using the concept of North African Dipole Intensity (NAFDI), which measures the intensity of the subtropical NAFH to the tropical low pressure of the monsoon. The NAFDI was previously used by Rodríguez et al. (2015) for studying three decades of dust export to the Atlantic, and by Cuevas et al. (2017) and Schepanski et al. (2017) for studying intraseasonal dust export. We determined the daily values of the NAFDI, using the NCEP/NCAR re-analysis data (Kalnay et al., 1996) as the difference of the anomalies of the daily values (d) of the 700hPa geo-potential height ($\Phi_{(d)}$) over Morocco (Mo, 30–32ºN, 5–8ºW) and Nigeria (Ni, 30–32ºN, 5–8ºE), with respect to the climatological (average) values from 1980 to 2010 ($\Phi_{(clim)}$; Cuevas et al., 2017):

$$NAFDI = \frac{1}{10}\left(\left(\Phi_{(d)} - \Phi_{(clim)}\right)_{Mo} - \left(\Phi_{(d)} - \Phi_{(clim)}\right)_{Ni}\right) \quad \text{Eq-1}$$

The selected point in Morocco is sensitive to the location (East-West shifts) of the NAFH (see M in Fig 1G), whereas the point in Nigeria is within a main path of the northward monsoon inflow (see N in Fig. 1D) associated with uplifting air (see N in Fig. 1F). We analysed the relationship between dust composition and NAFDI in two periods: August 2010 (Fig.6B1-6H1) and August 2013 (Fig.6B2-6H2).

Daily dust concentrations at Izaña Observatory are positively correlated with the daily values of NAFDI (lag -1; Figure 6B1 and 6B2), indicating that positive values of this index are associated with enhanced dust export to the subtropical North Atlantic. Fig. 7 shows the average meteorological fields (Fig. 7A-7E) and Dust Optical Depth (Fig. 7F) during the negative and positive phases of the NAFDI; results are consistent with those obtained by Cuevas et al. (2017) and Schepanski et al. (2017). Cuevas et al. (2017) showed that the changes of phase of NAFDI are connected with the mid latitude Rossby waves. The change of phase of NAFDI (negative to positive) is associated with a westward shift of the NAFH (centred over Tunisia in the NAFDI negative phase, Fig.7A1, and shifted to Morocco in the NAFDI positive phase, Fig.7A2) and a westward propagation of the Harmattan Band from Eastern Algeria - Libya (Mediterranean inflow, Kallos et al., 1998; Fig.7B1) to the

Atlantic coast of the Western Sahara (Fig.7B2). The change of NAFDI negative to positive is associated with a westward propagation of the dusty air mass within North Africa (Fig.7B1 to 7B2). The enhanced dust export that we observe to the Mediterranean during negative NAFDI (Fig. 7F1) was previously found by Cuevas et al. (2017) and Schepanski et al. (2017). Cuevas et al. (2017) also described the westward shift of the SHL that we observe when the NAFDI changes from negative (Fig.7C1-7D1) to positive (Fig.7C2-7D2) phase (also linked to enhanced deep convection in Mauritania, Fig.7E1-7E2), which is associated with the westward propagation of cooler Mediterranean air in the Harmattan Band (Fig.7B1-7B2). Analogously, Wang et al. (2017) also observed a reinforcement of the NAFH during the westward shift of the SHL.

The meteorological changes in North Africa associated with the change of phase of NAFDI have implications for the three large dust sources in western North Africa (PSA 1-3 highlighted in Fig.7B1-7B2) and on the composition of the dust exported in the SAL. Fig.6 shows bulk dust concentrations (Fig.6B1) and the ratios of Fe/Al, Ca/Al, K/Al, Na/Al, Mg/Al and S/Al (Fig.6C1-6H1) in the SAL (measured at Izaña) versus daily NAFDI (lag -1) values during our study period, August 2010. In order to verify if the observed relationships were observed in other periods, we performed a similar analysis with a data set collected in August 2013 Fig. (6B2-6H2). Increasing values of NAFDI (in the positive range) are correlated with higher dust concentrations in the SAL (Fig.6B1-6B2), with an increase in the Fe/Al ratio (dust richer in Fe, Fig.6C1-6C2), and with a decrease in the ratios of Ca, K, Na, Mg and S to Al (Fig.6D-6H). In summary, moderate values of NAFDI (0 to +2.5) are associated with Ca, K, Na, Mg and S rich dust in the SAL linked to Northern Saharan sources (northern PSA1 and PSA2; Fig.2C and Fig.4-4H), whereas higher NAFDI values (2.5 to +4) are associated with Fe rich dust from Southern Saharan regions (PSA3; Fig.2C and 4C)

These results are consistent with our previous meteorological description (Fig.7). This interpretation is also supported by the detailed meteorological analysis that we did for each of the events E1 to E6 shown on top of Fig.3B. Three brief examples:

- Event E1 (Fig. 8). Calcium rich dust impacted on Izaña the 24-Aug 2010 (Fig. 3B). Dust mobilization started the 19-Aug at PSA1 (Fig. 8A1 and Fig.11A; NE Algeria to Tunisia). The dusty air mass shifted westward across North Africa (Fig. 8A1-8F1, back-trajectory plotted in white colour; the arrow points to the daily location of the airmass) linked to a westward shift of the NAFH (Fig. 9A3-9F3), the Harmattan Band (Fig. 8A2-8F2), the SHL (Fig. 8A5-8F5) and the uplifting monsoon inflow south of the ITCZ (Fig. 8A4-8F4), in a sequence similar to that described above. The evolution of

the NAFDI values (change from - to +) is indicated on the top right side of plots of Fig. 8A1-8F1.

- Event E2 (Fig.9). Na and Cl rich dust (Fig. 3E and 3F) impacted at Izaña on the 26 Aug 2010. The surge of dust emissions occurred in northern edge of PSA2 (Bechar basin, border between Algeria and Morocco; Fig. 9A1-9A2), where the previous cited Yermosol occurs, in a scenario (Fig.11B) similar to that described by Fiedler et al. (2013) and Rodríguez et al. (2011). Again, a westward shift of the Harmattan Band and the NAFH (Fig.9B1-9B3 and 9C1-9C3) prompted dust export to the Atlantic.
- Event E5 (Fig. 10) impacted at Izaña on the 27 and 28 Aug 2010 (Fig 3B). This is the only case in which an impact of Si rich (Si/Al: 2.12; Fig. 3H), Fe rich (Fe/Al: 0.51; Fig. 3I), linked to hematite rich dust of western-PSA3, and Ca and S depleted dust (Fig. 3B-3C) was recorded. Dust uplift was linked to a deep convective cell that propagated, within the monsoon inflow (Fig. 10C-10D), from Mali to Mauritania (Fig. 10A1-10D1) in a scenario similar to those described by Marsham et al. (2008) and Bou Karam et al. (2008). Enhanced dust export is clearly observed in the satellite Dust Optical Depth (Fig.10A1 and 10D1). It is associated with a westward shift of the NAFH (Fig 10A3-10D3), of the monsoon inflow (purple contour of the negative omega domain; Fig 10A4-10D4) and of the SHL region (Fig 11C-11D); all these movements were traced by the increasing values of the NAFDI (top right of plots Fig. 10A1-10D1), from +1.76 to +2.86 (lag -1).

4. Conclusions

The high temporal resolution measurements performed in this study shows that dust composition in the Saharan Air Layer (SAL) experiences rapid variations, induced by the (meteorologically modulated) alternated impacts of different regional sources of North African dust. Dust composition (ratios of elements to Al) in the SAL experiences a significant variability in a few (5 to 8) hours, in such a way that, up to eight impacts of three of the large North African dust sources (NE Algeria, Western Sahara to Bechar region and Southern Sahara - Sahel) may occur in less than 1 week. The mobilization of dust from the different sources is associated with the westward propagating Harmattan pulses, the associated westward shifts of the Saharan Heat Low and convection, including processes embedded within the monsoon inflow. The North African Dipole Intensity (NAFDI: strength of the subtropical North African High, at Morocco, to the monsoon tropical low at Nigeria) traces the observed variability in dust composition. Moderate values of NAFDI (0 to +2.5) are associated with Ca, K, Na, Mg and S rich dust (linked to Northern Sahara sources) in the Atlantic SAL, higher NAFDI values (2.5 to 4) are associated with Fe rich

dust in the SAL (linked to Southern Sahara), whereas negative values of NAFDI promoted (Ca, K, Na, Mg and S rich) dust export to the Mediterranean. Trace metals (Br, Cr, Ni, Zn and Zr) are influenced by industrial emissions in North Africa.

5. Acknowledgements

This study was performed within the project VARDUST-SAL (PGC2018-099166-B-I00), funded by the Ministry of Science, Research and Innovation of Spain, the Research State Agency of Spain and the European Regional Development Fund (ERDF). JLD is awarded with a posdoc contract Agustín de Bethencourt, funded by the Program Fomento de Transferencia del Conocimiento, funded by the Cabildo de Tenerife. A stage of JLD at the INFN was funded by the Universidad de La Laguna. The authors gratefully acknowledge (i) the NOAA Air Resources Laboratory for providing the HYSPLIT transport and dispersion model, (ii) the NOAA NCEP Reanalysis data provided by the NOAA/OAR/ESRL PSD, Boulder, Colorado, USA, from their Web site at https://www.esrl.noaa.gov/psd/ and (iii) the Giovanni online data system, developed and maintained by the NASA GES DISC. We also thank to Dr. Albert Solé for his useful comments on soils and sabhkas.

6. References

Alfaro, S.C., Lafon, S., Rajot, J.L., Formenti, P., Gaudichet, A., Maille, M., 2004. Iron oxides and light absorption by pure desert dust: An experimental study. J. Geophys. Res. 109, D08208.

Allen, C.J.T., Washington, R., 2013. The low-level jet dust emission mechanism in the central Sahara: observations from Bordj-Badji Mokhtar during the June 2011 fennec intensive observation period. J. Geophys. Res. 119, 2990-3015.

Andreae, M.O., Rosenfeld, D. Aerosol–cloud–precipitation interactions. Part 1, 2008. The nature and sources of cloud-active aerosols. Earth-Science Reviews 89, 13–41.

Atkinson, J., Murray, B. J., Woodhouse, M. T., Whale, T. F., Baus- tian, K. J., Carslaw, K. S., Dobbie, S., O'Sullivan, D., Malkin, T. L., 2013. The importance of feldspar for ice nucleation by mineral dust in mixed-phase clouds, Nature, 498, 355–358.

Brindley, H. E. and J. E. Russell, 2009. An assessment of Saharan dust loading and the corresponding cloud-free longwave direct radiative effect from geostationary satellite observations, J. Geophys. Res., 114, 148-227.

Boose, Y., Sierau, B., García, M. I., Rodríguez, S., Alastuey, A., Linke, C., Schnaiter, M., Kupiszewski, P., Kanji, Z. A., and Lohmann, U., 2016. Ice nucleating particles in the Saharan Air Layer, Atmos. Chem. Phys., 16, 9067-9087.

Bou Karam, D., C. Flamant, P. Knippertz, O. Reitebuch, J. Pelon, M. Chong, A. Dabas, 2008. Dust emissions over the Sahel associated with the West African monsoon intertropical discontinuity region: A representative case-study. Q. J. R. Meteorol. Soc. 134, 621–634.

Bozlaker, A., Prospero, J.M., Price, J., Chellam, S., 2018. Linking Barbados mineral dust aerosols to North African sources using elemental composition and radiogenic Sr, Nd, and Pb isotope signatures. Journal of Geophysical Research123, 1384–1400.

Calzolai G., Chiari M., Lucarelli F., Nava S., Portarena S., 2010. Proton induced X-ray emission yields for the analysis of light elements in aerosol samples in an external beam set-up. Nuclear Instruments and Methods in Physics Research B 268, 1540–1545.

Calzolai G., Lucarelli F., Chiari M., Nava S., Giannoni M., Carraresi L., Prati P., Vecchi R., 2015. Improvements in PIXE analysis of hourly particulate matter samples. Nuclear Instruments and Methods in Physics Research B 363, 99–104.

Caquineau, S., Gaudichet, A., Gomes, L., Magonthier, M.C., Chatenet, B., 1998. Saharan dust: clay ratio as relevant tracer to assess the origin of soil derived aerosols. Geophyical Research Letters 27 983-986.

Claquin T., Schulz M., Balkanski Y. J., 1999. Modeling the mineralogy of atmospheric dust sources. Journal Geophysical Research, 104, D18, 22243-22256.

Cuesta, J., John, H., Marsham, H., Parker, D.J., Flamant, C., 2009. Dynamical mechanisms controlling the vertical redistribution of dust and the thermodynamic structure of the West Saharan atmospheric boundary layer during summer. Atmos. Sci. Let. 10, 34–42.

Cuevas, E., Gómez-Peláez, A.J., Rodríguez, S., Terradellas, E., Basart, S., García, R.D., García, O.E., Alonso-Pérez, S., 2017. The pulsating nature of large-scale Saharan dust transport as a result of interplays between mid-latitude Rossby waves and the North African Dipole Intensity. Atmos. Environ. 167, 586-602.

D'Alessandro, A., Lucarelli, F., Mandò, P.A., Marcazzan, G., Nava, S., Prati, P., Valli, G., Vecchi, R., Zucchiattia, A., 2003. Hourly elemental composition and sources identification of fine and coarse PM10 particulate matter in four Italian towns. Journal of Aerosol Science 34, 243-259.

De Menocal, P. B., Tierney, J. E., 2012. Green Sahara: African Humid Periods Paced by Earth's Orbital Changes. Nature Education Knowledge 3, 10-12.

García, M. I., Rodríguez, S., Alastuey, A., 2017. Impact of North America on the aerosol composition in the North Atlantic free troposphere, 2017. Atmos. Chem. Phys., 17, 7387-7404.

Engelstaedter, S., Washington, R., 2007. Atmospheric controls on the annual cycle of North African dust, J. Geophys. Res., 112, D03103.

Engelstaedter, S., Washington, R., Flamant, C., Parker, D. J., Allen, C. J. T., Todd, M. C., 2015. The Saharan heat low and moisture transport path- ways in the central Sahara—Multiaircraft observations and Africa-LAM evaluation, J. Geophys. Res. 120, 4417–4442.

Evan, A.T., Flamant, C., Gaetani, M., Guichard, F. 2016. The past, present and future of African dust. Nature 531, 493-495.

Fehlberg, H., Stahr, K., 1985. Development of sustained land use by understanding soil and landscape formation in the desert fringe area of NW-EGYIW. Catena 12, 307-328.

Fiedler, S., Schepanski, K., Heinold, B., Knippertz, P., Tegen, I., 2013. Climatology of nocturnal low-level jets over North Africa and implications for modeling mineral

624 dust emission. J. Geophys. Res., 118, 6100–6121.

625 Flamant, C., Chaboureau, J.P., Parker, D. J., Taylor, C. M., Cammas, J.P., Bock, O., Timouke,
626 F., Pelon, J., 2007. Airborne observations of the impact of a convective system on
627 the planetary boundary layer thermodynamics and aerosol distribution in the
628 inter-tropical discontinuity region of the West African Monsoon. Q. J. R. Meteorol.
629 Soc. 133, 1175–1189.

630 Font-Tullot, I.: Las invasiones de aire caliente africano en el Archipiélago Canario, Revista
631 de Geofísica, Vol. IX, 36, 334–349, 1950.
632 Formenti, P., Rajot, J. L., Desboeufs, K., Caquineau, S., Chevaillier, S., Nava, S., Gaudichet, A.,
633 Journet, E., Triquet, S., Alfaro, S., Chiari, M., Haywood, J., Coe, H., Highwood, E.,
634 2008. Regional variability of the composition of mineral dust from western Africa:
635 Results from the AMMA SOP0/DABEX and DODO field campaigns, J. Geophys. Res.,
636 113, D00C13.
637 Formenti, P., Nava, S., Prati, P., Chevaillier, S., Klaver, A., Lafon, S., Mazzei, F., Calzolai, G.,
638 Chiari, M., 2010. Self-attenuation artefacts and correction factors of light element
639 measurements by X-ray analysis: Implication for mineral dust composition studies,
640 J. Geophys. Res., 115, D01203.
641 Ginoux, P., Prospero, J. M., Gill, T. E., Hsu, N. C., Zhao, M., 2015. Global-scale attribution of
642 anthropogenic and nat- ural dust sources and their emission rates based on MODIS
643 Deep Blue aerosol products, Rev. Geophys., 50, RG3005..
644 Hamdi-Aissa, B., Valles, V., Aventurier, A., Ribolzi, O. 2004. Soils and brine geochemistry
645 and mineralogy of hyperarid desert playa, Ouargla basin, Algerian Sahara. Arid
646 Land, Research and Management 18, 103–126.
647 Hsu, N.C., Jeong, M.J., Bettenhausen, C., Sayer, A.M., Hansell, R., Seftor, C.S., Huang, J., Tsay,
648 S.C., 2013. Enhanced deep blue aerosol retrieval algorithm: the second generation.
649 J. Geophys. Res. 118.
650 Huneeus, N., Schulz, M., Balkanski, Y., Griesfeller, J., Prospero, J., Kinne, S., Bauer, S.,
651 Boucher, O., Chin, M., Dentener, F., Diehl, T., Easter, R., Fillmore, D., Ghan, S., Ginoux,
652 P., Grini, A., Horowitz, L., Koch, D., Krol, M. C., Landing, W., Liu, X., Mahowald, N.,
653 Miller, R., Morcrette, J.-J., Myhre, G., Penner, J., Perlwitz, J., Stier, P., Takemura, T.,
654 and Zender, C. S., 2011. Global dust model intercomparison in AeroCom phase I,
655 Atmos. Chem. Phys., 11, 7781–7816, doi:10.5194/acp-11-7781-2011.
656 Ito, A. Feng, Y., 2010. Role of dust alkalinity in acid mobilization of iron, Atmos. Chem.
657 Phys. 10, 9237-9250.
658 Jones, C., Mahowald, N., Luo, C., 2003. The role of easterly waves on African desert dust
659 transport, J. Climate, 16, 3617–3628.
660 Journet E., Balkanski Y., Harrison S.P., 2014. A new data set of soil mineralogy for dust-
661 cycle modeling, Atmos. Chem. Phys. 14, 3801-3816.
662 Kalnay, E., Kanamitsu, M., Kistler, R., Collins, W., Deaven, D., Gandin, L., Iredell, M., Saha, S.,
663 White, G., Woollen, J., Zhu, Y., Leetmaa, A., Reynolds, R., Chelliah, M., Ebisuzaki, W.,
664 Hig- gins, W., Janowiak, J., Mo, K. C., Ropelewski, C., Wang, J., Jenne, R., Joseph, D.,
665 1996. D. The NCEP/NCAR 40-Year Reanalysis Project, B. Am. Meteorol. Soc., 77,
666 437–471.

667 Kallos, G., Kotroni, V., Lagouvardos, K., Papadopoulos, A., 1998. On the long range
668 transport of air pollutants from Europe to Africa. Geophysical Research Letters 25,
669 5, 619-622.
670 Kandler, K., Benker, N., Bundke, U., Cuevas, E., Ebert, M. , Knippertz, P., Rodríguez, S.,
671 Schütz, L., Weinbruc, S., 2007. Chemical composition and complex refractive
672 index of Saharan Mineral Dust at Izaña, Tenerife (Spain) derived by electron
673 microscopy. Atmos. Environ. 41, 8058–8074.
674 Kandler, K., Schütz, L., Deutscher, C., Ebert, M., Hofmann, H., Jäckel, S., Jaenicke, R.,
675 Knippertz, P. Lieke, K., Massling, A., Petzold, A., Schladitz, A., Weinzierl, A.,
676 Wiedensohler, A., Zorn, S., Weinbruch, S., 2009. Size distribution, mass
677 concentration, chemical and mineralogical composition and derived optical
678 parameters of the boundary layer aerosol at Tinfou, Morocco, during SAMUM
679 2006. Tellus 61B, 32–50.
680 Knippertz, P., Deutscher, C., Kandler, K., Müller, Schulz, O., Schütz, L., 2007. Dust
681 mobilization due to density currents in the Atlas region: Observations from the
682 Saharan Mineral Dust Experiment 2006 field campaign, J. Geophys. Res., 112,
683 D21109.
684 Knippertz, P., 2008. Dust emissions in the West African heat trough – the role of the
685 diurnal cycle and of extratropical disturbances. Meteorologische Zeitschrift, Vol.
686 17, No. 5, 553-563.
687 Lammel, G., Röhrl, A., Schreiber, H., 2002. Atmospheric Lead and Bromine in Germany
688 Post-abatement Levels, Variabilities and Trends. Environ Sci & Pollut Res 9, 397 –
689 404.
690 Lavaysse, C., Flamant, C., Janicot, S., Parker, D.J., Lafore, J.-P., Sultan, B., Pelon, J., 2009.
691 Seasonal evolution of the West African heat low: a climatological perspective. Clim.
692 Dyn. 33, 313-330.
693 Legrand, M.; Plana-Fattori, A.; N'doumé, C., 2001. Satellite detection of dust using the IR
694 imagery of Meteosat 1. Infrared difference dust index, J. Geophys. Res., Vol. 106,
695 18251–18274
696 Levy, R.C., Remer, L.A., Kleidman, R.G., Mattoo, S., Ichoku, C., Kahn, R., Eck, T.F., 2010.
697 Global evaluation of the Collection 5 MODIS dark-target aerosol products over
698 land. Atmos. Chem. Phys. 10, 10399-10420.
699 Lucarelli F., Calzolai G., Chiari M., Giannoni M., Mochi D., Nava S., Carraresi L., 2014. The
700 upgraded external-beam PIXE/PIGE set-up at LABEC for very fast measurements
701 on aerosol samples. Nuclear Instruments and Methods in Physics Research B 318,
702 55-59.
703 Lucarelli F., Calzolai G., Chiari M., Nava S., Carraresi L., 2018. Study of atmospheric aerosols
704 by IBA techniques: The LABEC experience. Nuclear Instruments and Methods in
705 Physics Research B 417, 121-127.
706 Maxwell A., Teesdale W.J., Campbell J.L., 1995. The Guelph PIXE software package II. Nucl.
707 Instr. Meth. B 95, 407.
708 Manson, B. 1966. Principles of Geochemistry. Wiley, New York.
709 Marsham, J. H., Parker, D. J., Grams, C. M., Taylor, C. M., Haywood, J. M., 2008 Uplift of
710 Saharan dust south of the intertropical discontinuity. Journal of Geophysical
711 Research, 113, D21102.

712 Middleton, J.L., Mukhopadhyay, S., Langmuir, C.H., McManus, J.F., Huybers, P.J., 2018.
713 Millennial-scale variations in dustiness recorded in Mid-Atlantic sediments from 0
714 to 70 ka. Earth and Planetary Science Letters, 482, 12-22, 2018.
715 Miller, R. L., Knippertz, P., Pérez García-Pando, C., Perlwitz, J.P., Tegen, I., 2014. Impact of
716 dust radiative forcing upon climate, in Mineral Dust: A Key Player in the Earth
717 System, edited by P. Knippertz and J.-B. W. Stuut, pp. 327-357, Springer, Dordrecht,
718 Netherlands.
719 Moreno, T., Querol, X., Castillo, S., Alastuey, A., Cuevas, E., Herrmann, L., Mounkaila, M.,
720 Elvira, J., Gibbons, W., 2006. Geochemical variations in aeolian mineral particles
721 from the Sahara–Sahel Dust Corridor. Chemosphere 65, 261–270.
722 Moskowitz, B.M., Reynolds, R.L., Goldstein, H.L., Berquó, T.S., Kokaly, R.F., Bristow, C.S.,
723 2016. Iron oxide minerals in dust-source sediments from the Bodélé Depression,
724 Chad: Implications for radiative properties and Fe bioavailability of dust plumes
725 from the Sahara. Aeolian Research 22, 93-106.
726 Nickovic, S., Vukovic, A., Vujadinovic, M., Djurdjevic, V., Pejanovic, G., 2012. Technical Note:
727 High-resolution mineralogical database of dust-productive soils for atmospheric
728 dust modeling, Atmos. Chem. Phys., 12, 845–855.
729 Pérez García-Pando, C., Miller, R. L. ,Perlwitz, J. P., Rodríguez, S., Prospero, J. M., 2016.
730 Predicting the mineral composition of dust aerosols: Insights from elemental
731 composition measured at the Izaña Observatory, Geophys. Res. Lett., 43.
732 Perlwitz, J. P., Pérez García-Pando, C., Miller, R. L., 2015 Predicting the mineral
733 composition of dust aerosols—Part 1: Representing key processes. Atmos. Chem.
734 Phys. 15, 11593-11627.
735 Prospero, J. M. and Carlson, T. N., 1972. Vertical and areal distribution of Saharan dust
736 over the western Equatorial North Atlantic Ocean, J. Geophys. Res., 77, 5255–5265.
737 Prospero, J. M., Ginoux, P., Torres, O., Nicholson, S. E., Gill, T. E., 2002. Environmental
738 characterization of global sources of atmospheric soil dust identified with the
739 Nimbus 7 Total Ozone Mapping Spectrometer (TOMS) absorbing aerosol product,
740 Rev. Geophys., 40, 1–31.
741 Ravelo-Pérez, L. M., Rodríguez, S., Galindo, L., García, M. I., Alastuey, A., López- Solano,
742 J., 2016. Soluble iron dust export in the high altitude Saharan Air Layer. Atmos.
743 Environ. 133, 49-59.
744 Reid, E. A., Reid, J. S., Meier, M. M., Dunlap, M. R., Cliff, S. S., Broumas, A., Perry, K., Maring,
745 H., 2003. Characterization of African dust transported to Puerto Rico by individual
746 particle and size segregated bulk analysis, J. Geophys. Res. 108, 8591.
747 Reynolds, R.L., Cattle, S.R., Moskowitz, B.M., Goldstein, H.L., Yauk, K., Flagg, C.B., Berquó,
748 T.S., Kokaly, R., Morman, S., Breit, G.N., 2014. Iron oxide minerals in dust of the Red
749 Dawn event in eastern Australia, September 2009. Aeolian Research 15, 1-13.
750 Rizzolo, J. A., Barbosa, C. G. G., Borillo, G. C., Godoi, A. F. L., Souza, R. A. F., Andreoli, R. V.,
751 Manzi, A. O., Sá, M. O., Alves, E. G., Pöhlker, C., Angelis, I. H., Ditas, F., Saturno, J.,
752 Moran-Zuloaga, D., Rizzo, L. V., Rosário, N. E., Pauliquevis, T., Santos, R. M. N.,
753 Yamamoto, C. I., Andreae, M. O., Artaxo, P., Taylor, P. E., Godoi, R. H. M., 2017
754 Soluble iron nutrients in Saharan dust over the central Amazon rainforest, Atmos.
755 Chem. Phys. 17, 2673-2687.
756 Rodríguez, S., Alastuey, A., Alonso-Pérez, S., Querol, X., Cuevas, E., Abreu-Afonso, J., Viana,
757 M., Pérez, N., Pandolfi, M., de la Rosa, J., 2011. Transport of desert dust mixed

with North African industrial pollutants in the subtropical Saharan Air Layer, Atmos. Chem. Phys. 11, 6663–6685.
Rodríguez, S., Alastuey, A., Querol, X., 2012. A review of methods for long term in situ characterization of aerosol dust, Aeolian Res. 6, 55–74.
Rodríguez, S., Cuevas, E., Prospero, J.M., Alastuey, A., Querol, X., Lopez-Solano, J., García, M.I., Alonso-Perez, S., 2015. Modulation of Saharan dust export by the North African dipole. Atmos. Chem. Phys. 15, 7471-7486.
Rodríguez, S., Calzolai, G., Chiari, M., Nava, S., García, M.I., López-Solano, J., Marrero, C., Cuevas, E., Alonso-Pérez, S., Prats, N., Amato, F., Lucarelli, F., Querol, X., 2019. High temporal resolution measurements of dust composition in the Saharan Air Layer – dataset. doi:
Schepanski, K., Heinold, B., Tegen, I., 2017. Harmattan, Saharan heat low, and West African monsoon circulation: modulations on the Saharan dust outflow towards the North Atlantic, Atmos. Chem. Phys., 17, 10223-10243.
Scheuvens, D., Schütz, L., Kandler, K., Ebert, M., Weinbruch, S., 2013. Bulk composition of northern African dust and its source sediments — A compilation. Earth-Science Reviews 116, 170–194.
Scott, J.R., 1952. A note on an intertropical discontinuity. Quarterly Journal of the Royal Meteorological Society, vol. 78, issue 338, pp. 621-624.
Skonieczny, C., Paillou, P., Bory, A., Bayon, G., Biscara, L., Crosta, X., Eynaud, F., Malaizé, B., Revel, M., Aleman, N., Barusseau, J.P., Vernet, R. Lopez, S., Grousset, F., 2015. African humid periods triggered the reactivation of a large river system in Western Sahara. Nature Communications 6, 8751.
Stein, A.F., Draxler, R.R., Rolph, G.D., Stunder, B.J.B., Ngan, F. Cohen, M.D., 2015. NOAA's HYSPLIT atmospheric transport and dispersion modelling system. Bulleting of American Meteorological Society, 96, 12 2059-2077.
Tsamalis, C., Chédin, A., Pelon, J., Capelle, V., 2013. The seasonal vertical distribution of the Saharan Air Layer and its modulation by the wind, Atmos. Chem. Phys., 13, 11235–11257.
UK Meteorological Office: Weather in the Mediterranean, Vol. I, 2nd Edition, General Meteorology HM Stat, Office, London, 1962.
Wang, W., Evan, A.T., Lavaysse, C., Flamant, C., 2017. The role the Saharan Heat Low plays in dust emission and transport during summertime in North Africa. Aeolian Research, 28, 1-12.
Zhang, X., Zhao, L., Tong, D.Q., Wu, G., Dan, M., Teng, B., 2016. A Systematic Review of Global Desert Dust and Associated Human Health Effects. Atmosphere, 7, 158.

795
796 Table 1. Ratio of elements to Al (based on 128 hourly samples) for major (Si to Cl,
797 μg/μg) and trace (Ti to Sr, ng/μg) elements registered in the dusty SAL from 24-
798 Aug 17h to 30-Aug 00h 2010 at Izaña Observatory. Includes percentiles 98th,
799 percentiles 2nd and average (arithmetic mean) for total particles. NOVAR (%) for
800 total, coarse and fine particles. NA: none available.

	total 98th	**total** 2nd	**total** average	**total** NOVAR, %	**coarse** NOVAR, %	**fine** NOVAR, %
Si	2.13	1.95	2.03	9	11	NA
Fe	0.51	0.46	0.48	9	11	18
K	0.24	0.19	0.21	25	26	42
Mg	0.29	0.23	0.25	25	32	36
Ca	0.74	0.37	0.47	79	107	76
S	0.19	0.06	0.12	111	172	119
Na	0.36	0.10	0.22	116	152	117
Cl	0.16	0.04	0.08	156	212	177
Ti	64.3	53.0	57.2	20	35	44
Mn	8.83	6.32	7.66	33	77	74
Sr	6.73	3.33	4.60	74	104	83

801
802
803 Table 2. Ratios of several elements to Al for major (Si to Cl, μg/μg) and trace
804 elements (Ti to Sr, ng/μg) measured in the dusty SAL at Izaña when the air mass
805 has passed by several potential source areas (PSA), according to the MRAR
806 analysis. Data extracted from the Median Ratios At Receptor matrix.
807

	PSA1	northern-PSA2	PSA3	PSA-in-Mo
Si	2.04	1.98	2.10	2.01
Fe	0.48	0.47	0.50	0.48
K	0.22	0.22	0.20	0.22
Mg	0.27	0.25	0.24	0.27
Ca	0.60	0.49	0.43	0.60
S	0.18	0.18	0.09	0.16
Na	0.24	0.30	0.15	0.26
Cl	0.07	0.14	0.05	0.09
Ti	55.0	57.0	57.0	57.0
Mn	8.3	7.0	8.3	7.7
Sr	6.0	5.0	4.0	6.0

808
809

Table 3. Properties of key minerals components of North African dust. Includes a qualitative description of the mass size distribution between the clays (with most of the mass < 2μm) and silt (with most of the mass between 2 to 60μm) size range typically used in modeling (source: Journet et al., 2014) and the ratios to Al of Al-bearing minerals determined using their empirical formulas (www.webmineral.com).

Mineral	clay size	silt size	Si/Al	Fe/Al	Mg/Al	K/Al	Ca/Al	Na/Al
Clay group:								
Illite	dominant	negligible	2.80	0.16	0.21	0.67		
Kaolinite	dominant	negligible	1.04					
Smectite group:	dominant	negligible						
Montmorillonite			2.08				0.07	0.09
Chlorite group:	present	present						
Clinochlore			1.56	1.29	1.69			
Chamosite			1.56	3.62	0.68			
Feldspar group:	minority	majority						
Orthoclase			3.12			1.45		
Evaporites group:								
Gypsum	minority	majority						
Calcite	present	present						
Dolomite	present	present						
Oxides group:								
Hematite	dominant	negligible						
Goethite	present	present						
Quartz	minority	majority						

Figures

Figure 1. A) Scatter plot of Aluminium vs PM_{10} concentrations in aerosol samples collected in the SAL at Izaña in August 2013. B) Picture of a PM_{10} aerosol sample collected in the SAL at Izaña is shown to illustrate the ochre colour. C) Back-trajectories to Izaña (red point) calculated for every hour of the study period, 23-Aug 19h to 30-Aug 17h 2010 (total: 166 back-trajectories). Key airflow (1.1 to 2) are highlighted with arrow. D) Back-trajectories density map (number of back-trajectory points that passed by each 1◦ × 1◦ degree pixel of the study domain) for the back-trajectories group (24-Aug 11h to 30-Aug 17h 2010) used for identifying the potential source areas. The industrial areas over Tunisia, Algeria and Morocco are plotted (see details in Rodríguez et al., 2011).

Figure 2. A) Dust Optical Depth (DOD) measured by MODIS (average 23-30 Aug 2010). B) dust record at Izaña and zonal component of the Harmattan wind in the Subtropical Saharan Stripe (SSS 25-28ºN, 7ºW-2ºE) from 1987 to 2017. Topographic (C1) and watershed (C2) maps showing the Potential Source Areas (PSA) of dust (Scheuvens et al., 2013). D-I) Mean meteorological fields (23-30 Aug 2010). Key components of the North African summer meteorology: Harmattan Band along the SSS (HB, white arrow), ITCZ (dotted white line), SHL, African Easterly Jet (AEJ) and the SAL is highlighted. Inner Morocco (in-Mo) potential source area cited in the text is highlighted. White line circles - M and N - highlights the location of the Morocco and Nigeria for the calculation of NAFDI.

Figure 3. Time series of hourly concentrations of dust (A) and of ratios (B-H) of several elements (Ca, S, Mg, Cl, Na, K, Si and Fe) to aluminium in total, coarse (2.5-10 μm) and fine (<2.5μm) dust fractions at Izaña Observatory from 23 Aug 19h to 30 Aug 17h 2010. Ratios are shown in the period when Izaña was impacted by the Saharan Air Layer.

Figure 4. Median Ratios At Receptor –MRAR- plots for several elements (Si, Ca, Fe, S, Mn, Sr, Na, Mg, Cl, Ti, K, Cu, Br, Cr, Ni, Zn and Zr) measured in the dusty SAL at Izaña (24-Aug 17h to 30-Aug 16h), based on 144 back-trajectories. The plots include the location of the potential source areas of dust (1, 2, 3 and In-Mo in A and G) and the location of the industrial (M).

Figure 5. Scatter plot of several elements to Al measured by PIXE in 1h resolution samples collected at Izaña Observatory with two streakers: one for total particles (first column) and other for coarse (central column) and fine (right column) particles. Blue dots in the plot of sulphur (C) indicates samples collected under dust free conditions (23 -16h- to 24 -16h- Aug 2010), previous to the dusty – SAL impact. The slopes (S1 to S3) indicate the different trends, since they are representative of the X/Al.

Figure 6. A) Location of three of the potential source areas (PSA) of dust in North Africa, Izaña and the two reference sites (M: Morocco and Nigeria) to calculate NAFDI. B-H) Concentrations of dust and elemental ratios to Aluminum (X/Al) versus daily NAFDI for 24-31 Aug 2010 (column 1, left) and 1-31 Aug 2013

(column 2, right). A decreasing scale is used for NAFDI to highlight the westward transport to the Atlantic (with respect to the PSA) under positive NAFDI values.

Figure 7. Meteorological fields (A-E) and satellite Dust Optical Depth (F) during negative (right column) and positive (left column) phases of NAFDI. HB: Harmattan Band. SHL: Saharan Heat Low. Vertical wind is shown in terms of omega parameter (negative and positive values indicate upward and downward movements, respectively).

Figure 8. Event E1 (24-Aug 16h- 25-Aug 01h 2010): Ca rich dust linked to transport from PSA1 to Izaña Observatory. The evolution (from 19-Aug to 24 Aug 2010) of the Dust Optical Depth and back-trajectory (A1-F1), horizontal wind at 850 hPa (A2-F2), height of the geopotential of 850 hPa (A3-F3), vertical wind at 850hPa (A4-F4) and thickness of the 1000-500 hPa layer (A5-F5) is shown. Column 1: white arrow indicates the track of the back-trajectory for each day. Column 2: white arrow highlights the Harmattan Band (HB). Column 3: H highlight the location of the core of the North African anticyclone. Column 4: vertical wind is shown in terms of omega parameter (negative and positive values indicate upward and downward movements, respectively). Daily value of NAFDI is shown on the right top of the plots of column 1. HB is also shown with arrow in column 2, 4 and 5.

Figure 9. Event E2 (25-Aug 18h – 26 Aug 07h 2010): transport of Cl and Na rich dust linked to transport from PSA2 to Izaña Observatory. The evolution (21-Aug to 23-Aug 2010) of the Dust Optical Depth and back-trajectory (A1-C1), horizontal wind at 925hPa (A2-C2) and height of the geopotential of 850hPa (A3-C3). Column 1: white arrow indicates the track of the back-trajectory for each day, white point position at 00h. Column 2: white arrow highlights the the Harmattan Band (HB). Column 3: H highlights the location of the core of the North African anticyclone. Daily value of NAFDI is shown on the top right of the plots of column 1.

Figure 10. Event E5 (27-Aug 22h – 28 Aug 13h 2010): transport of Fe rich dust from PSA3 to Izaña Observatory. The evolution (25-Aug to 28-Aug 2010) of the Dust Optical Depth and back-trajectory (A1-D1), horizontal wind at 850hPa (A2-D2), height of the geopotential of 850hPa (A3-D3), vertical wind (A4-D4) and temperature at surface (A5-D5). Column 1: white arrow indicates the track of the back-trajectory for each day. Column 2: the location of the Harmattan Band (HB) is highlighted. Column 3: H highlights the location of the core of the North African anticyclone. Column 4: vertical wind component is shown in terms of the omega parameter (negative and positive values indicate upward and downward movements, respectively). Daily value of NAFDI is shown on the top right of the plots of column 1.

Figure 11. Satellite dust observations based on SEVIRI infrared (10.8 μm) product (A and C) and Aerosol Optical Depth – SEVIRI based (B and D) during dust events occurring the 19 (18h), 22 (10h), 25(12h) and 25(13h) of Aug 2010. Arrows show the direction of transport of dust.

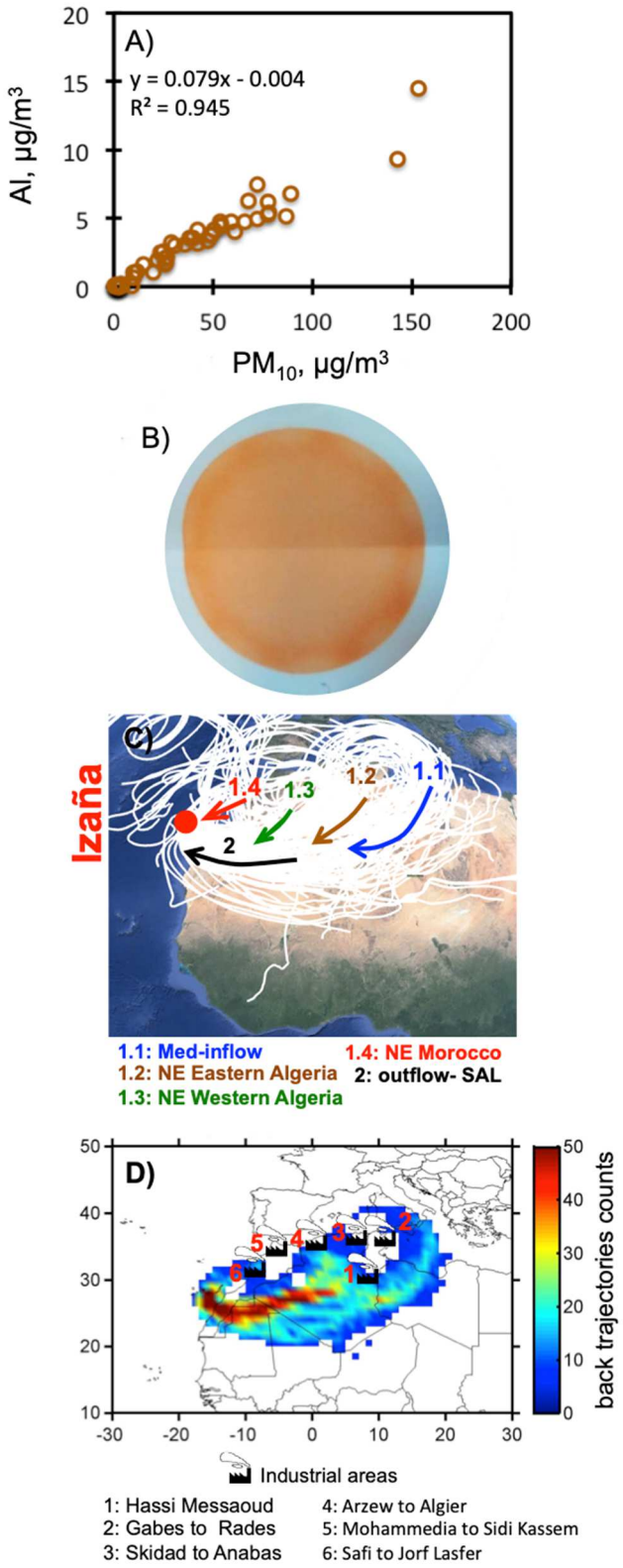
A)
y = 0.079x - 0.004
R² = 0.945
Al, µg/m³
PM10, µg/m³
B)
C)
Izaña
1.1
1.2
1.3
1.4
2
1.1: Med-inflow
1.2: NE Eastern Algeria
1.3: NE Western Algeria
1.4: NE Morocco
2: outflow- SAL
D)
back trajectories counts
Industrial areas
1: Hassi Messaoud
2: Gabes to Rades
3: Skidad to Anabas
4: Arzew to Algier
5: Mohammedia to Sidi Kassem
6: Safi to Jorf Lasfer

Figure 1

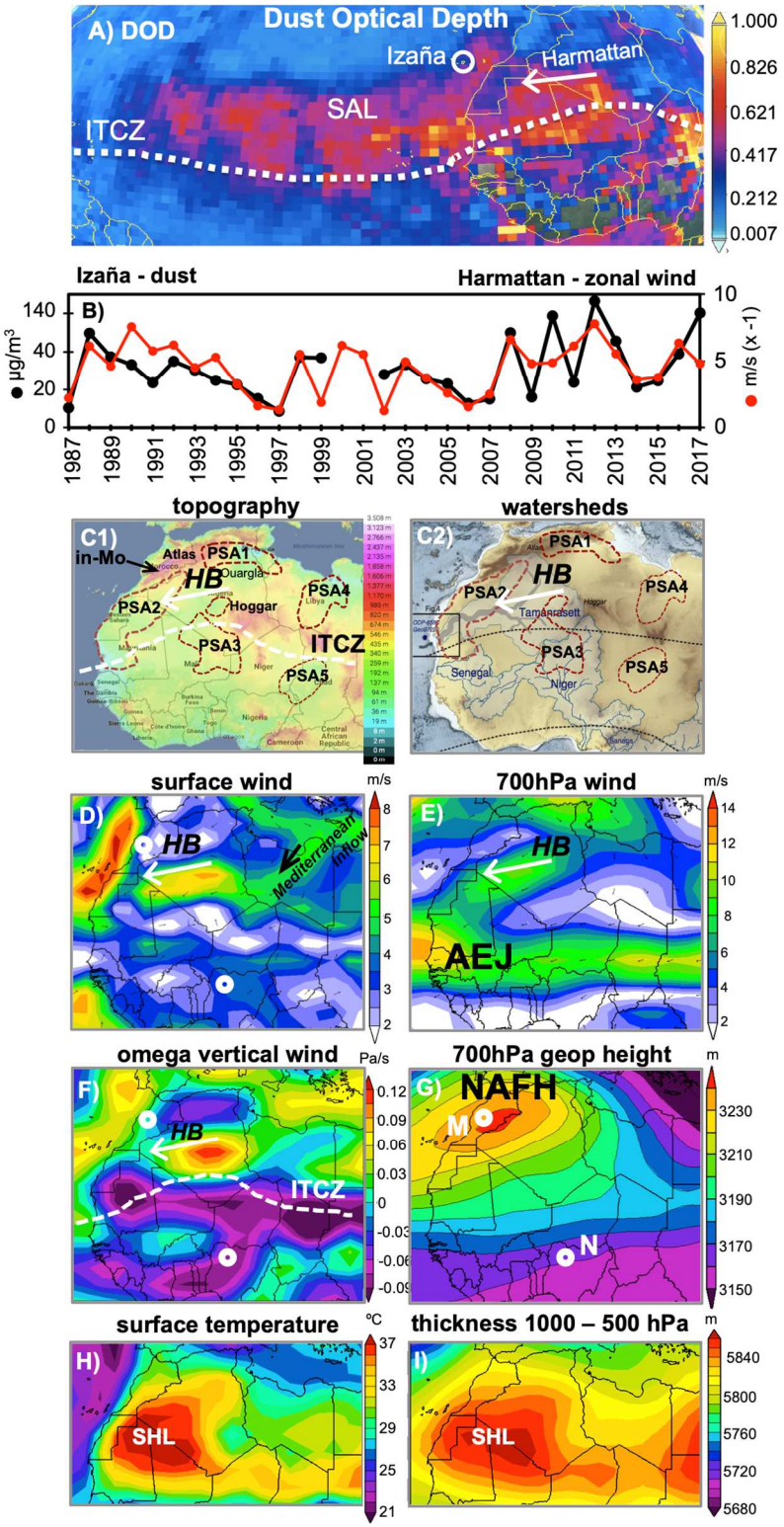
A) DOD
Dust Optical Depth
Izaña
Harmattan
SAL
ITCZ
1.000
0.826
0.621
0.417
0.212
0.007
Izaña - dust
Harmattan - zonal wind
B)
140
40
20
0
µg/m³
10
5
0
m/s (x -1)
1987
1989
1991
1993
1995
1997
1999
2001
2003
2005
2007
2009
2011
2013
2015
2017
topography
watersheds
C1)
in-Mo
Atlas
PSA1
HB
Ouargla
PSA2
Hoggar
PSA4
PSA3
ITCZ
PSA5
C2)
PSA1
HB
PSA7
PSA4
Tamanrasett
PSA3
PSA5
Senegal
Niger
surface wind
m/s
D)
HB
Mediterranean inflow
700hPa wind
m/s
E)
HB
AEJ
omega vertical wind
Pa/s
F)
HB
ITCZ
0.12
0.09
0.06
0.03
0
-0.03
-0.06
-0.09
700hPa geop height
m
G)
NAFH
M
N
3230
3210
3190
3170
3150
surface temperature
°C
H)
SHL
37
33
29
25
21
thickness 1000 – 500 hPa
m
I)
SHL
5840
5800
5760
5720
5680

Figure 2

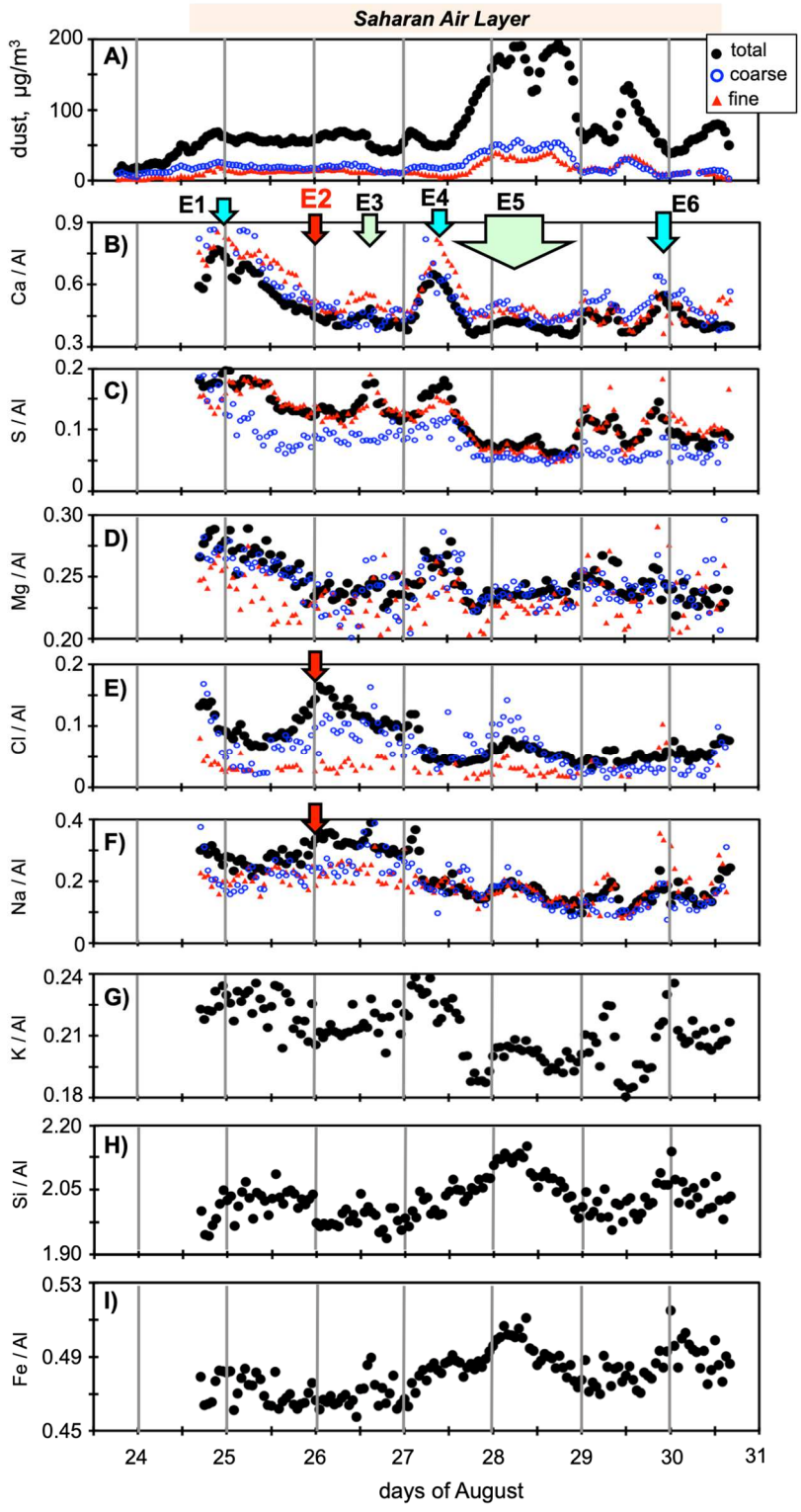
Saharan Air Layer
A)
dust, µg/m³
200
100
0
total
coarse
fine
E1
E2
E3
E4
E5
E6
B)
Ca / Al
0.9
0.6
0.3
C)
S / Al
0.2
0.1
0
D)
Mg / Al
0.30
0.25
0.20
E)
Cl / Al
0.2
0.1
0
F)
Na / Al
0.4
0.2
0
G)
K / Al
0.24
0.21
0.18
H)
Si / Al
2.20
2.05
1.90
I)
Fe / Al
0.53
0.49
0.45
24
25
26
27
28
29
30
31
days of August

Figure 3

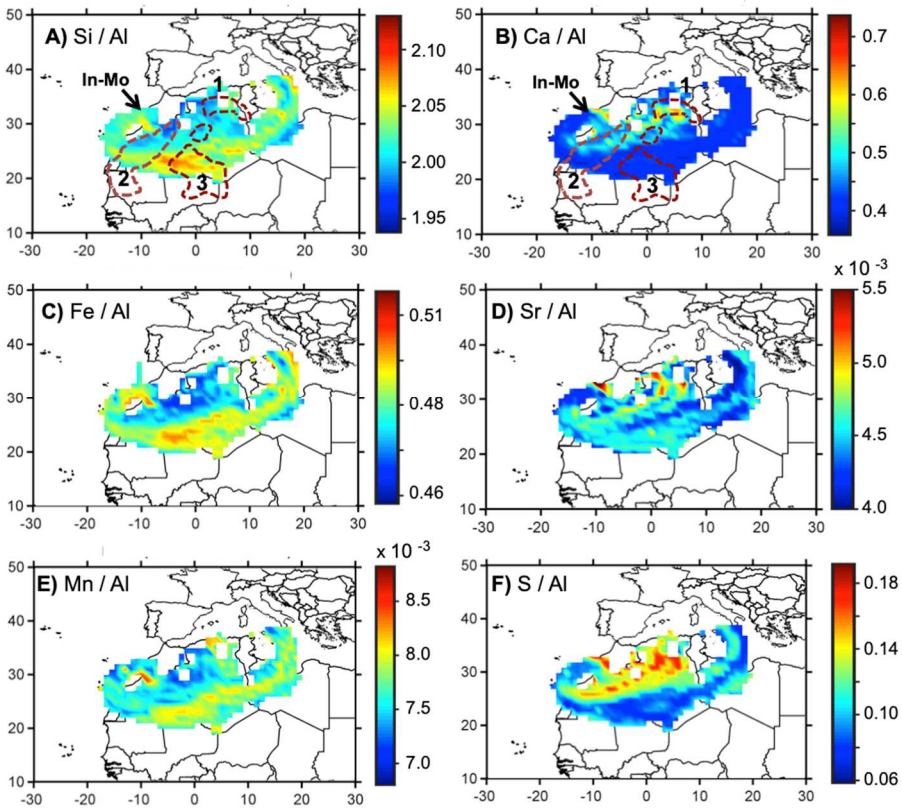
A) Si / Al
In-Mo
1
2
3
2.10
2.05
2.00
1.95
B) Ca / Al
In-Mo
1
2
3
0.7
0.6
0.5
0.4
C) Fe / Al
0.51
0.48
0.46
D) Sr / Al
x 10 -3
5.5
5.0
4.5
4.0
E) Mn / Al
x 10 -3
8.5
8.0
7.5
7.0
F) S / Al
0.18
0.14
0.10
0.06

Figure 4

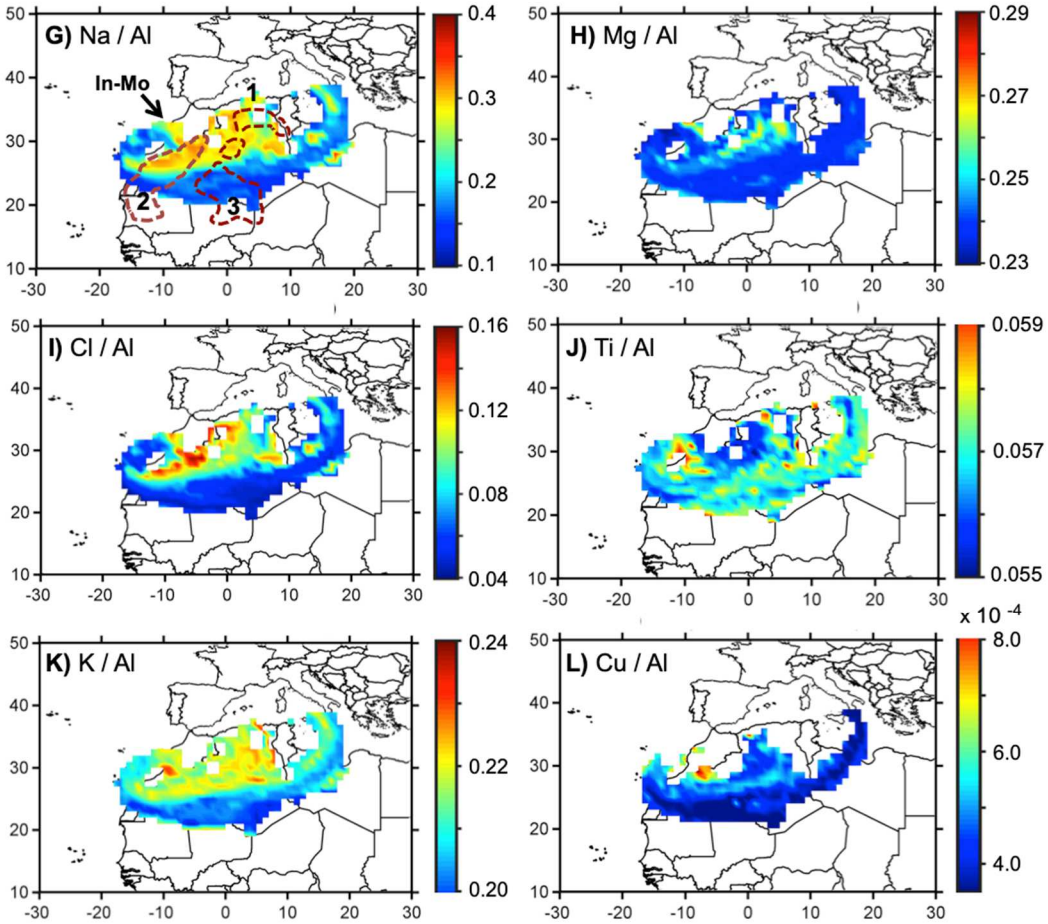

Figure 4 (continue)

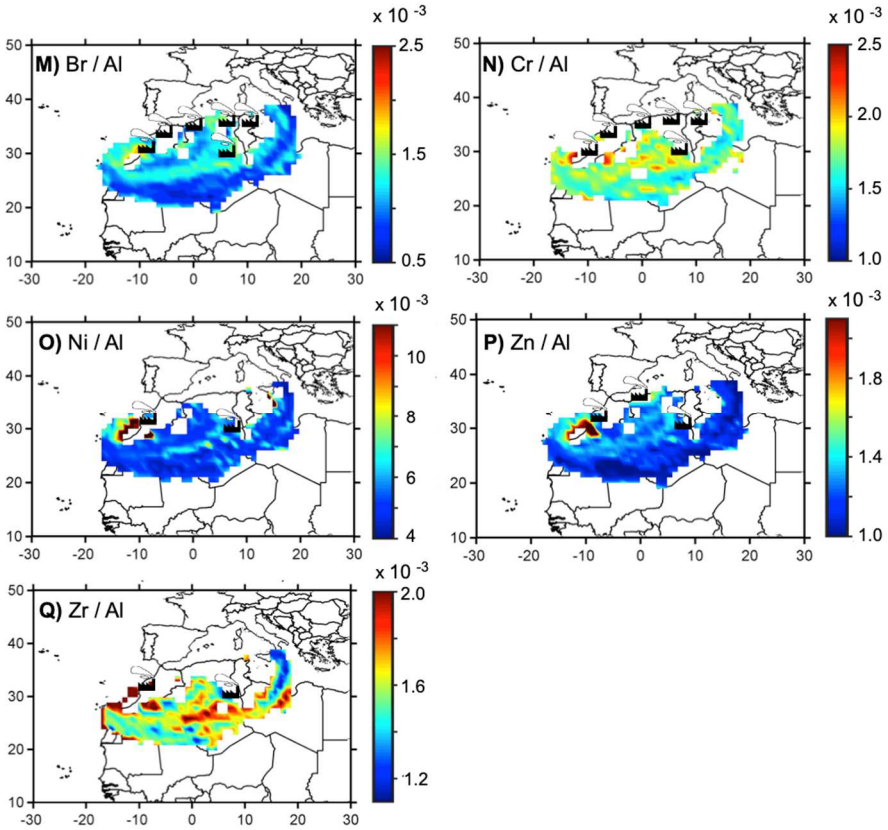

Figure 4 (continue)

951

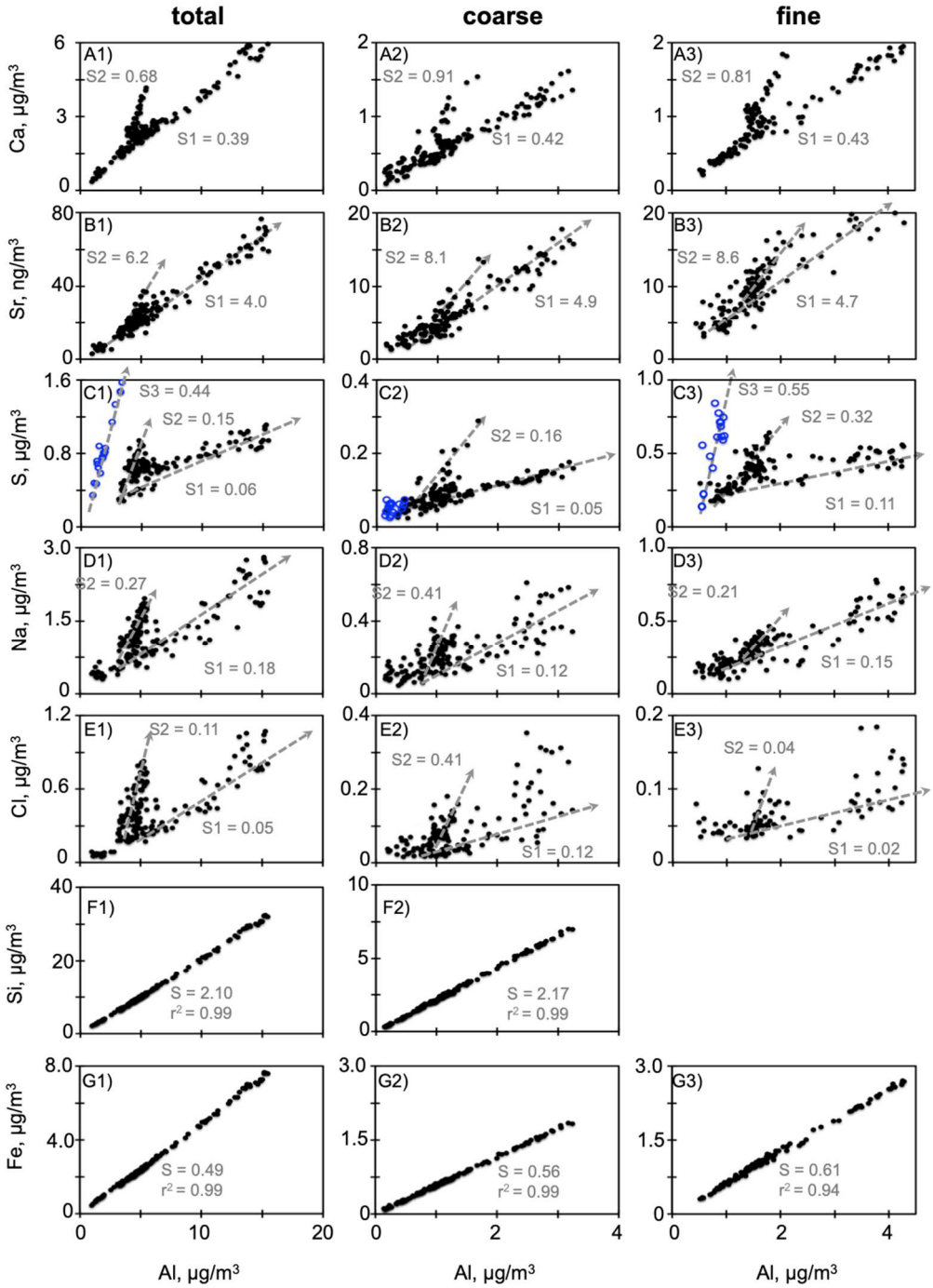

952
953 Figures 5
954
955

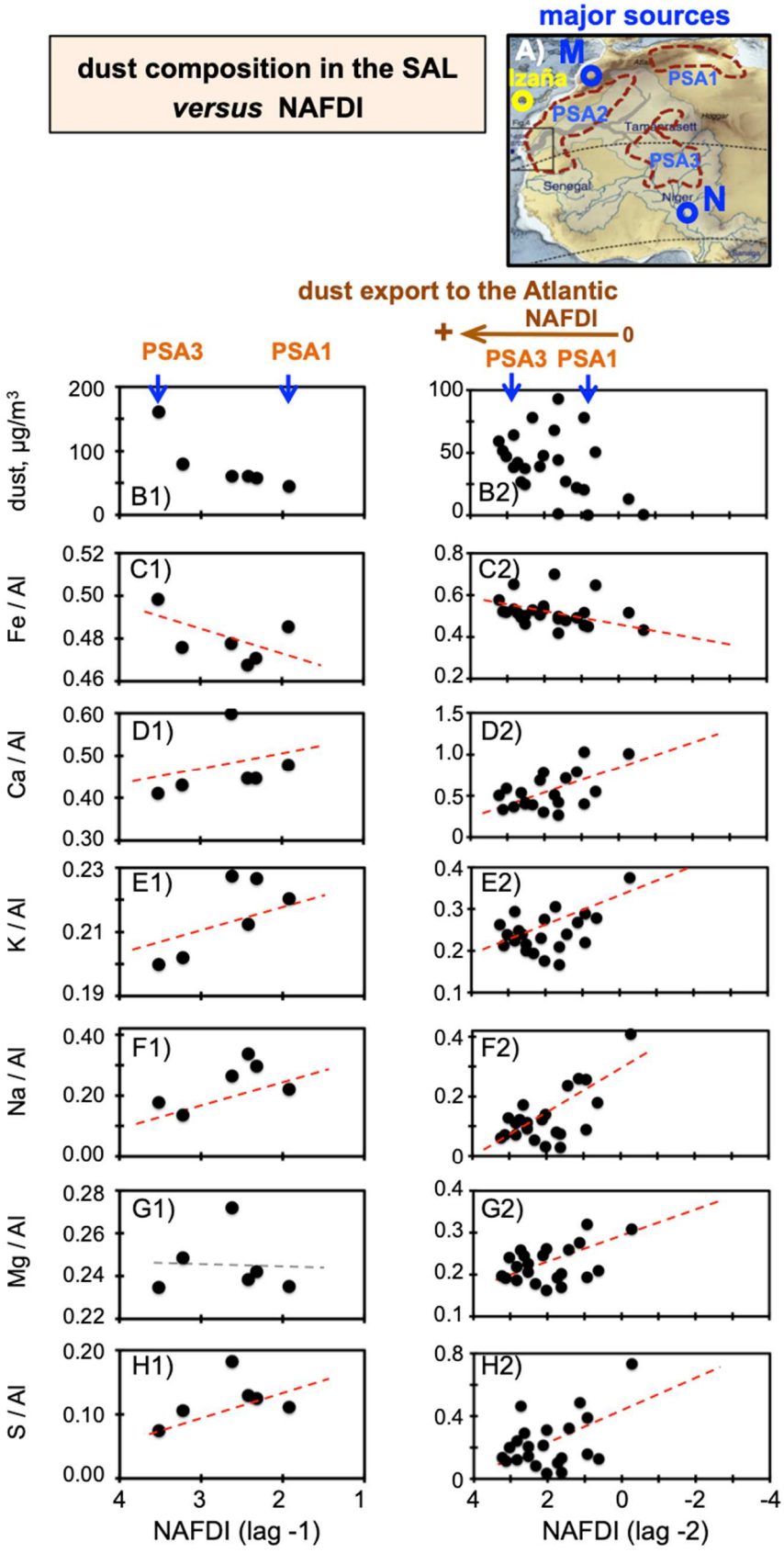
dust composition in the SAL
versus NAFDI
major sources
A)
M
Izaña
PSA1
PSA2
PSA3
Senegal
Niger
N
dust export to the Atlantic
NAFDI
+
0
PSA3
PSA1
dust, µg/m³
B1)
B2)
Fe / Al
C1)
C2)
Ca / Al
D1)
D2)
K / Al
E1)
E2)
Na / Al
F1)
F2)
Mg / Al
G1)
G2)
S / Al
H1)
H2)
NAFDI (lag -1)
NAFDI (lag -2)

Figure 6

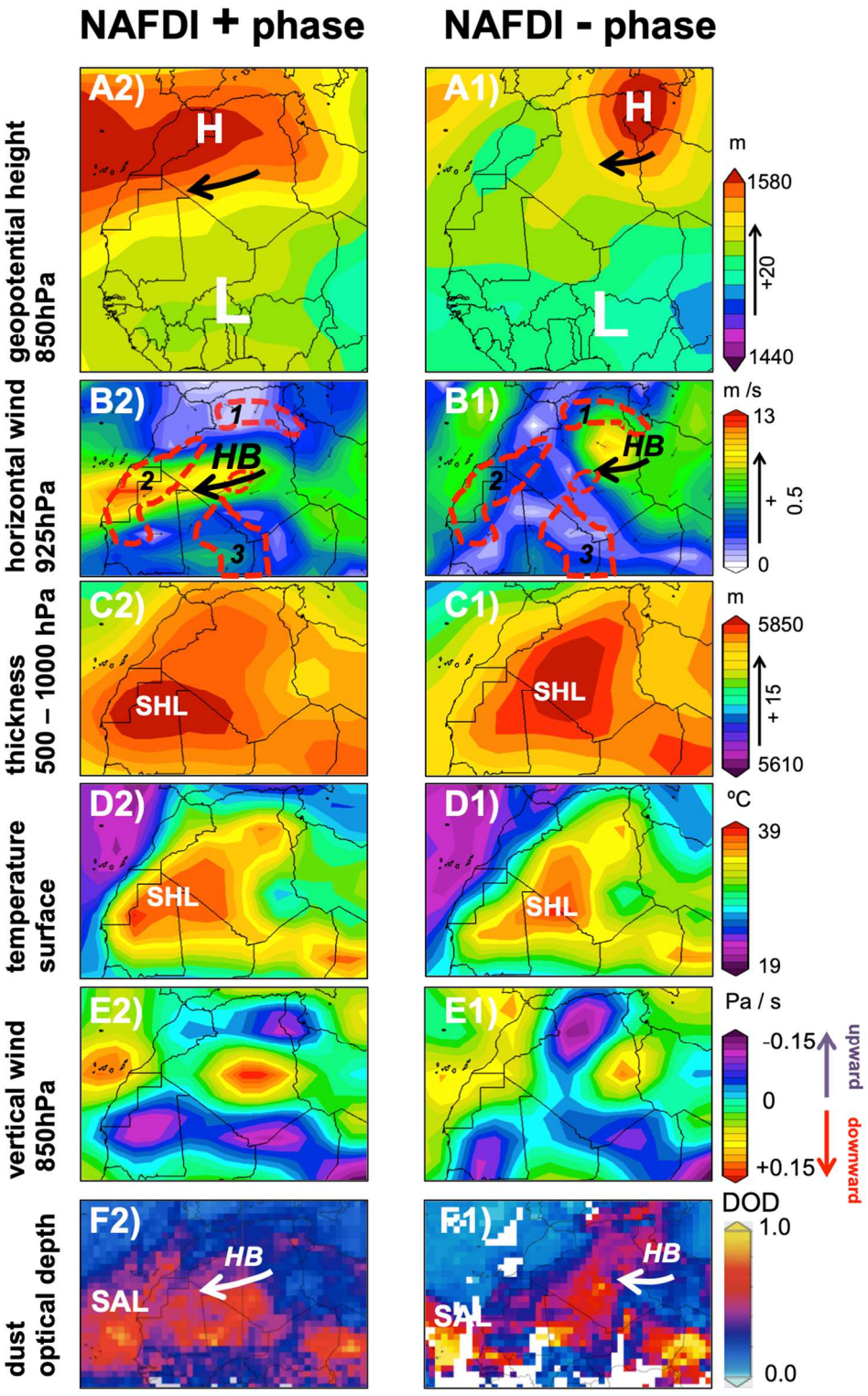
NAFDI + phase
NAFDI - phase
geopotential height 850hPa
horizontal wind 925hPa
thickness 500 – 1000 hPa
temperature surface
vertical wind 850hPa
dust optical depth
A2)
A1)
H
L
m
1580
+20
1440
B2)
B1)
1
2
3
HB
m /s
13
+ 0.5
0
C2)
C1)
SHL
m
5850
+ 15
5610
D2)
D1)
°C
39
19
E2)
E1)
Pa / s
-0.15
0
+0.15
upward
downward
F2)
F1)
SAL
DOD
1.0
0.0

Figure 7

964

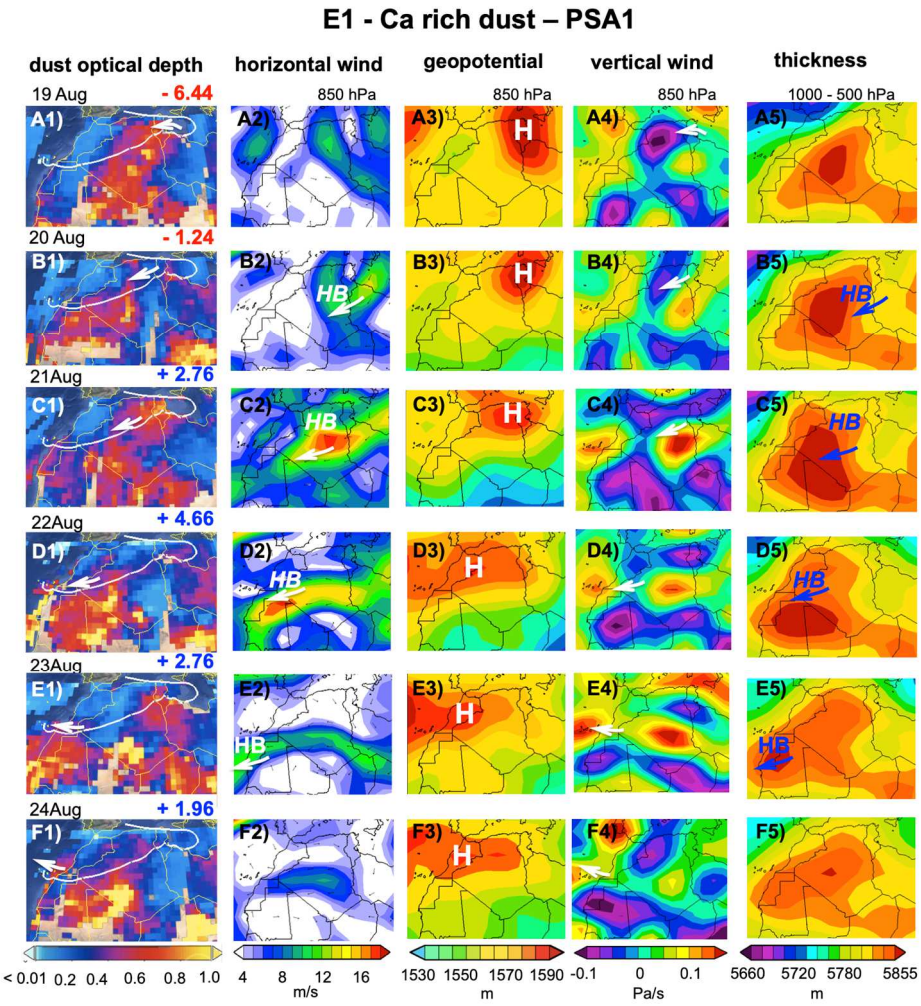

965
966 Figure 8
967

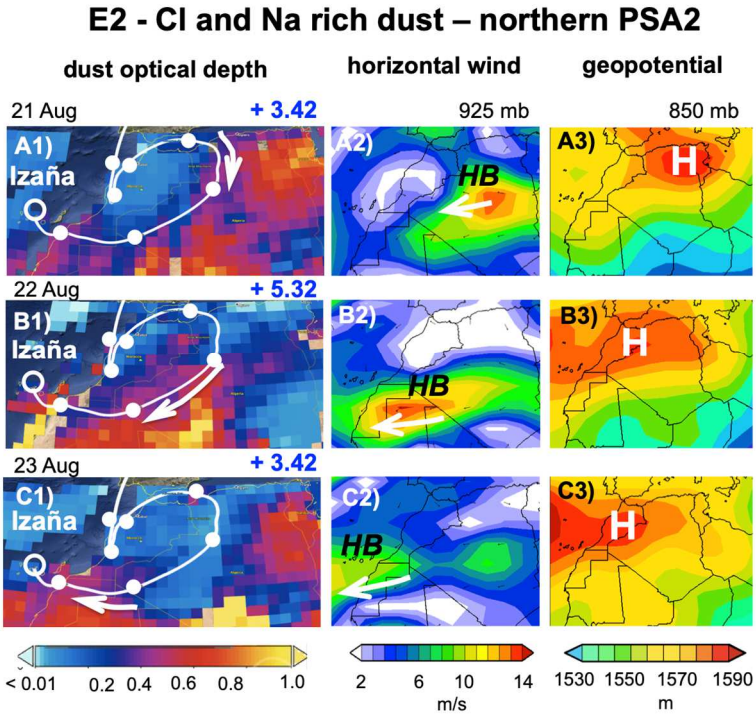
E2 - Cl and Na rich dust – northern PSA2
dust optical depth
horizontal wind
geopotential
21 Aug
+ 3.42
925 mb
850 mb
A1)
Izaña
A2)
HB
A3)
H
22 Aug
+ 5.32
B1)
Izaña
B2)
HB
B3)
H
23 Aug
+ 3.42
C1)
Izaña
C2)
HB
C3)
H
< 0.01
0.2
0.4
0.6
0.8
1.0
2
6
10
14
m/s
1530
1550
1570
1590
m

Figure 9

975

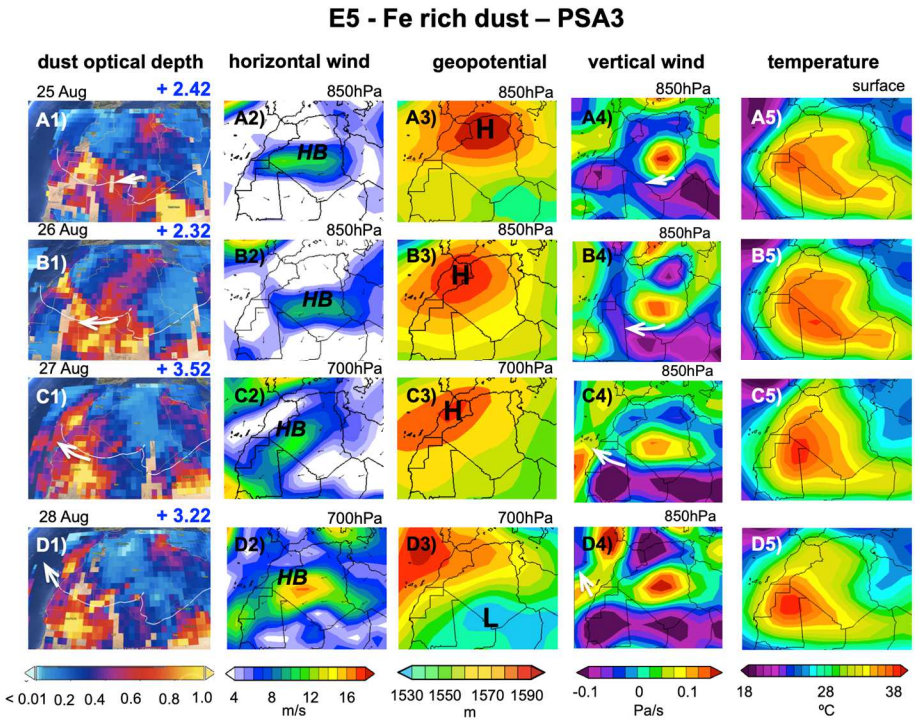

976
977 Figure 10
978

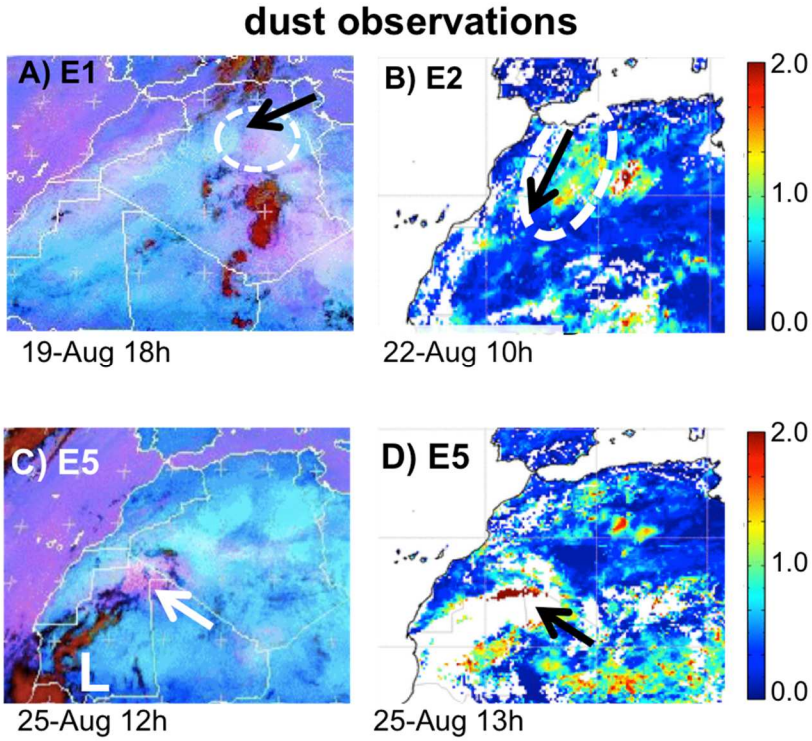
dust observations
A) E1
19-Aug 18h
B) E2
22-Aug 10h
2.0
1.0
0.0
C) E5
L
25-Aug 12h
D) E5
25-Aug 13h
2.0
1.0
0.0

Figure 11

Graphical abstract